

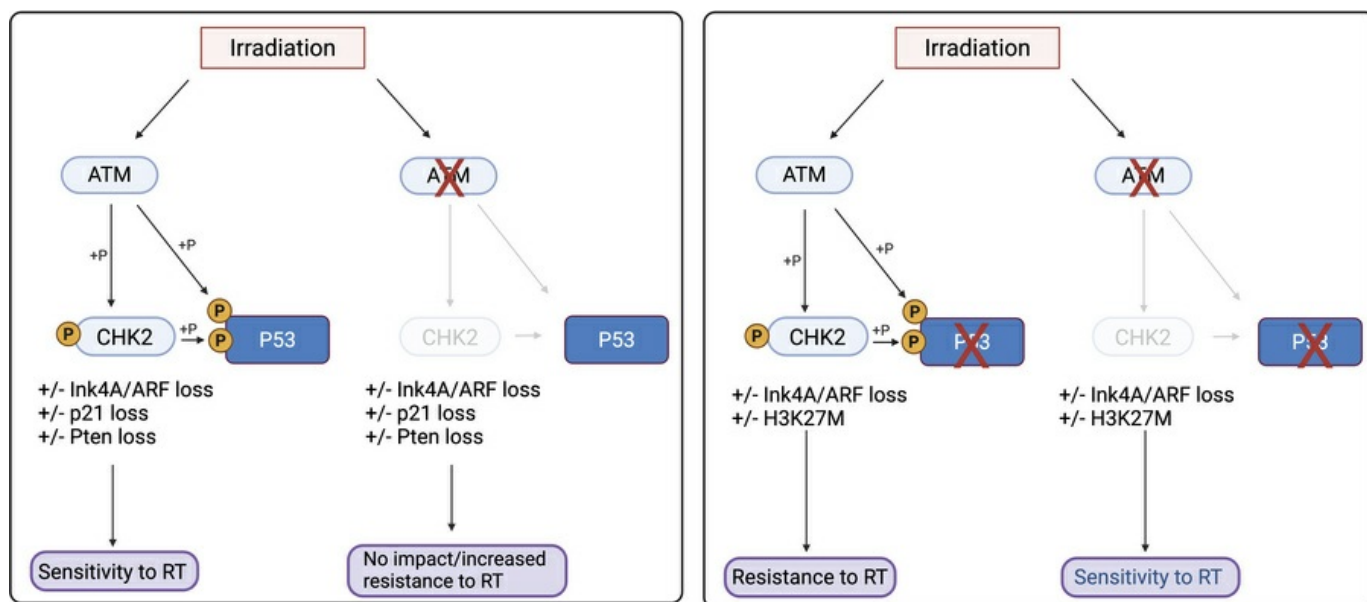
Disruption of Ataxia-telangiectasia mutated kinase enhances radiation therapy efficacy in spatially-directed diffuse midline glioma models

Avani Mangoli, ... , Simon G. Gregory, Zachary J. Reitman

J Clin Invest. 2025. <https://doi.org/10.1172/JCI179395>.

Research In-Press Preview Neuroscience Oncology

Graphical abstract



Find the latest version:

<https://jci.me/179395/pdf>



Disruption of Ataxia telangiectasia mutated kinase enhances radiation therapy efficacy in spatially-directed diffuse midline glioma models.

Author List based on Contribution:

Avani Mangoli*¹

Vennesa Valentine*²

Spencer Maingi²

Sophie R. Wu²

Harrison Q. Liu²

Michael Aksu³

Vaibhav Jain³

Bronwen E. Foreman²

Joshua A. Regal²

Loren B. Weidenhammer²

Connor E. Stewart²

Maria E. Guerra Garcia²

Emily Hocke²

Karen Abramson³

Tal Michaeli¹

Nerissa T. Williams²

Lixia Luo²

Megan Romero⁴

Katherine Deland²

24 Samantha Gadd⁵
25 Eita Uchida⁵
26 Laura Attardi⁶
27 Kouki Abe⁵
28 Rintaro Hashizume⁵
29 David M. Ashley¹
30 Oren J. Becher⁴
31 David G. Kirsch⁷
32 Simon G. Gregory^{3**}
33 Zachary J. Reitman^{2***}

34

35 *Co-First Author

36 **Co-Corresponding Author

37

38 ***Corresponding author

39

40 **Corresponding Author:**

41 Zachary J. Reitman, MD, PhD

42 30 Duke Medicine Circle, Box 3085,

43 Durham, 27710, NC, USA

44 Email: zjr@duke.edu

45 Phone: (919) 668-7336

46

47
48
49
50
51
52
53
54
55
56
57
58
59
60
61
62
63
64
65
66
67
68
69

Co-corresponding author:

Simon G. Gregory, PhD
300 N. Duke Street, DUMC 104775
Durham, 27701, NC, USA
Email: simon.gregory@duke.edu
Phone: (919) 684-0726

¹The Preston Robert Tisch Brain Tumor Center, Duke University, Durham, North Carolina, United States 27710

²Department of Radiation Oncology, Duke University, Durham, North Carolina, United States 27710

³The Preston Robert Tisch Brain Tumor Center Omics Program, Duke University, Durham, North Carolina, United States 27710

⁴Department of Pediatric Hematology Oncology, Mount Sinai Kravis Children's Hospital, 1468 Madison Avenue, New York, NY, United States 10029

⁵Department of Pediatrics, University of Alabama at Birmingham, Birmingham, Alabama, United States 35233

⁶Departments of Radiation Oncology and Genetics, Stanford University School of Medicine, 269 Campus Drive, Stanford, California, United States 94305-5152

⁷Princess Margaret Cancer Centre, University of Toronto, 610 University Avenue, Toronto, Ontario, Canada M5G 2M9

Abstract:

Diffuse midline gliomas (DMGs) are lethal brain tumors characterized by p53-inactivating mutations and oncohistone H3.3K27M mutations that rewire the cellular response to genotoxic stress. We used RCAS/tv-a retroviruses and Cre recombinase to inactivate p53 and induce native H3.3K27M mutations in a lineage- and spatially-directed manner. We generated primary mouse tumors that recapitulate human DMG. Disrupting ataxia-telangiectasia mutated kinase (ATM) enhanced the efficacy of radiation therapy in murine and patient-derived DMG models which increased survival.. Microscopy-based in situ sequencing was used to spatially resolve transcriptional profiles in >750,000 single cells with or without ATM disruption and radiation therapy, revealing altered immune-neoplastic and endothelial cell interactions after treatment. An allelic series of primary murine DMG models with different p53 mutations confirmed that transactivation-independent p53 activity is a key mediator of radiosensitivity after ATM disruption. Our findings contribute primary DMG mouse models with deep profiling and reveal the mechanisms of treatment response to an actionable therapeutic strategy.

Introduction

Diffuse midline gliomas (DMGs) are lethal brain tumors in children and young adults. These tumors are localized in essential midline brain structures, such as the brainstem and thalamus, making them surgically inoperable and unresponsive to conventional chemotherapy. The median overall survival of patients with DMGs is less than two years. Although radiation therapy may improve symptoms and extend life, it remains palliative. Somatic activation of lysine 27 to methionine mutations in histone variant 3.3 (H3.3K27M) is a defining feature of DMG (1, 2). Approximately 70% of DMGs harbor inactivating mutations in the tumor suppressor *TP53* (1-3), which are associated with radioresistance in patients and preclinical models (4, 5).

A key limitation of current primary DMG preclinical models is the ability to induce K27M mutations in the native *H3f3a* locus in a spatial-, lineage-, and temporally controlled manner. Patient-derived xenografts (6), patient-derived cell lines (7), *in utero* electroporation (7), and syngeneic mouse models (8, 9) have provided key insights into this disease. A conditional H3f3a-loxP-Stop-loxP-K27M-Tag allele (H3f3a^{LSL-K27M-Tag}) has also been generated that allows the expression of H3.3K27M from the endogenous mouse *H3f3a* locus in the presence of Cre recombinase (10). However, this model has been limited by cell lineages that can be interrogated with existing Cre driver lines, such as *Nestin*-Cre (10). To date, the conditional H3.3K27M alleles have not been investigated in an entirely spatially controlled manner. We and others have used the RCAS/tv-a retroviral system for spatially-directed modulation of glioma tumorigenesis in mice (5, 11-15). The RCAS/tv-a platform was used to deliver an exogenous H3.3K27M

(13, 14, 16), but to our knowledge it has not been used to edit the endogenous *H3f3a* allele. A variety of model systems have been used to investigate the mechanisms associated with the development of DMG and to assess therapeutic strategies.

Inhibition of ataxia-telangiectasia mutated kinase (ATM) has emerged as a strategy to enhance the efficacy of radiation therapy in DMG (17). ATM is a master orchestrator of the DNA damage response to double strand breaks (17). Patients with hereditary loss-of-function ATM variants, and tumors containing ATM variants, are extremely sensitive to radiation therapy (17). Consequently, a brain-penetrant ATM inhibitor has entered clinical trials for adult brain tumors (NCT03423628) (18). A recent study identified ATM inhibition as a potent radiosensitization strategy in various patient-derived pediatric high-grade glioma models (6). We found that functional ATM loss radiosensitized primary mouse models of DMG were driven by p53 loss, but not p53 wildtype (5, 11). ATM loss increases tumor sensitivity to radiotherapy via radiosensitization of neoplastic cells rather than the vasculature (12). However, it remains uncertain whether H3.3K27M affects the ability of *Atm* loss to radiosensitize primary DMG. This is of particular importance since H3.3K27M regulates the p16 molecular checkpoint that regulates G1-to-S cell cycle progression (13) and could thereby influence the radiation response.

Here, we examined strategies to exploit the genomically-stressed cell state in H3.3K27M/TP53-altered DMG. We improved upon previous models that delivered H3.3K27M from an exogenous RCAS payload (11, 13) by combining the RCAS/tv-a system with H3f3a^{LSL-K27M-Tag} mice to express H3.3K27M from the endogenous *H3f3a*

locus. This autochthonous mouse model enabled us to analyze the impact of *Atm* loss in the context of H3.3K27M/TP53-altered brain tumors to mimic human DMG (10). We found that primary DMGs expressing H3.3K27M driven by p53 loss were radiosensitized by *Atm* loss. To explore the resistance mechanisms in specific tumor cells, we examined primary mouse DMGs after focal brain irradiation using high-resolution single cell *in situ* sequencing (ISS). The results identified the overexpression of the cell cycle regulator *Cdkn1a* as a putative resistance factor in *Atm*-intact DMG. We showed that *Cdkn1a*, or the transcriptional activity of p53 in general, was dispensable for DMG radiosensitization by *Atm* loss. Therefore, the non-transactivation functions of p53 may determine the sensitivity of DMGs to combinations of ATM inhibitors and radiation therapy. The high-resolution results describe a genetically faithful and flexible primary mouse model of DMG, identifying the mechanisms of resistance to a therapeutic strategy currently in clinical trials.

Results

Conditional p53 loss and H3.3K27M expression in retrovirus-induced mouse

DMGs.

To express H3.3K27M from the endogenous *H3f3a* locus in retrovirus-induced primary mouse gliomas, we used a $H3f3a^{LSL-K27M-Tag}$ allele that expresses H3.3K27M in the presence of Cre recombinase (10). To incorporate the $H3f3a^{LSL-K27M-Tag}$ allele into the RCAS/tv-a retrovirus system, mice were bred with $Nestin^{TVA}$ mice to allow RCAS retroviruses to specifically transduce TVA+ *Nestin*-expressing neural stem cells. To investigate the deletion of p53 specific to tumors, we crossbred a p53 variant in which critical exons were flanked by loxP sites (floxed or FL) allowing for functional deletion of p53 in the presence of Cre recombinase. We first introduced retroviruses into $Nestin^{TVA}$; $p53^{FL/FL}$; $H3f3a^{LSL-K27M-Tag/+}$ mice (nPH) and compared them to matched mice lacking the $H3f3a^{LSL-K27M-Tag}$ allele (nP, Figure 1A). We induced DMGs by injecting mice with RCAS retroviruses expressing Cre recombinase, firefly luciferase, and the oncogene platelet-derived growth factor ligand beta (PDGF-B) and monitored for tumor formation via *in vivo* imaging. Using luciferase-based bioluminescent imaging to detect tumors, we determined that there was no difference in time to tumor formation in $H3f3a^{LSL-K27M-Tag/+}$ mice compared to matched mice lacking the $H3f3a^{LSL-K27M-Tag}$ allele (Figure 1B). To investigate the effects of *Atm* deletion in these tumors, we also generated $Nestin^{TVA}$; $p53^{FL/FL}$; $H3f3a^{LSL-K27M-Tag}/+;$ $Atm^{FL/FL}$ (nPHA^{FL/FL}) mice and littermate controls with intact *Atm* in their tumors of genotype $Nestin^{TVA}$; $p53^{FL/FL}$; $H3f3a^{LSL-K27M-Tag}/+;$ $Atm^{FL/+}$ (nPHA^{FL/+}) (Figure 1C-E, see description of *Atm* loss results below). Tumors exhibiting hypercellularity and diffuse infiltration of the nearby normal brain on H&E formed within

171 4-8 weeks with high penetrance (Figure 1F). We detected HA expression indicating the
172 presence of the HA tag on both H3.3K27M and PDGF-B constructs (Figure 1G). As
173 expected, p53 was not detected in p53^{FL/FL} tumors by IHC (Figure 1H). Histone 3 lysine
174 27 trimethylation was significantly decreased by IHC in H3f3a^{LSL-K27M-Tag} /+ tumors
175 compared to controls (mean 50.49 % (nP) vs. 5.757 % (nPH) of cells staining positive,
176 p-value <0.001, Figure 1I and Supplemental Figure 1), indicating that H3.3K27M could
177 functionally deplete H3K27me3 as predicted (19). Differentially methylated features
178 between nP versus K27M-bearing tumors showed hyper- and hypo- methylated
179 features within promoters (Supplemental Figure 2A) and enhancers (Supplemental
180 Figure 2B) Additional analysis shows a difference in percentage of methylation within
181 hypomethylated tiles and de-novo tiles in K27M tumors compared to nP and normal
182 murine tissue (Supplemental Figure 2C and D). Differentially methylated genes yielded
183 from the hypomethylated genomic regions were most enriched for processes involving
184 neuronal development and differentiation, suggesting developmental properties for
185 promoter and enhancer tiles (Supplemental Figure 2E). This finding is consistent with
186 other tissues DNA methylation state of these specific tiles and with the role of K27M in
187 regulating oncogenic and developmental processes (20) Sequence motif analysis
188 identified differential methylation of motifs associated with transcription factors Hoxd13
189 and Hoxa11 (Supplemental Figure 2F) which are known to be involved in hindbrain
190 development. Ki67 was elevated in >50% of tumor cells regardless of H3.3K27M status
191 (Figure 1J). Anti-Flag immunohistochemistry confirmed the presence of the Flag tag on
192 the H3.3K27M construct (Figure 1K). Flag IHC demonstrated that H3.3K27M-Tag+ cells
193 diffusely infiltrated from a hypercellular tumor core into the brain parenchyma

suggesting the diffuse, infiltrative biology seen in human DMG. These results demonstrate that RCAS/tv-a and a conditional H3f3a^{LSL-K27M-Tag} allele can be combined to target K27M to *H3f3a* gene in time, lineage, and space to generate primary mouse DMGs that recapitulate human disease.

***Atm* loss radiosensitizes primary p53-null/H3.3K27M DMGs.**

Targeting ATM kinase has emerged as a potential strategy to increase the efficacy of standard-of-care radiation therapy for brain tumors (5, 6, 17). We sought to determine whether disruption of ATM could radiosensitize primary mouse DMGs with p53 and H3.3K27M alterations. Previously, we established that *H3f3a*-wildtype brainstem gliomas lacking *Atm* in tumor cells were radiosensitized compared to littermate controls with a functional *Atm* allele in their tumors(5). However, these mice lack H3.3K27M which disrupts the G1-to-S cell cycle checkpoint (13) and may thereby affect the downstream effects of ATM deficiency (17). We hypothesized that *Atm* inactivation in the presence of the H3.3K27M allele would also radiosensitize tumors. To test this, we examined the tumor-free survival of nPHA^{FL/FL} mice and compared them to controls with intact ATM in their tumors of genotype nPHA^{FL/+} (Figure 1C). There was no difference in tumor-free survival between nPHA^{FL/FL} and nPHA^{FL/+} mice in the absence of irradiation (Figure 1D). To test whether *Atm* deletion radiosensitizes p53-null/H3.3K27M DMGs, we delivered three daily fractions of 10 Gy focal brain irradiation to mice using the Small Animal Radiation Research Platform (SARRP). nPHA^{FL/FL} mice had significantly longer median survival than nPHA^{FL/+} mice (P-value=0.03 using Mantel Cox (log rank test), Figure 1E). Thus, *Atm* deletion in tumor cells enhances the efficacy of focal brain

irradiation for primary p53-null/H3.3K27M DMGs. H&E confirmed tumor (Figure 1F) followed by IHC confirming HA expression (Figure 1G), p53 loss (Figure 1H), the presence of H3.3K27M (Figure 1I), Ki67 (Figure 1J) and anti-FLAG (Figure 1K). These results show that *Atm* disruption enhances the efficacy of radiation therapy for primary mouse DMGs that contain p53 loss and the H3.3K27M mutation.

In situ multiplexed microscopy reveals cell cycle and Semaphorin pathway changes after irradiation and *Atm* disruption.

To explore the mechanisms underlying radiation efficacy and resistance, we performed spatially resolved gene expression analyses of primary mouse DMGs. Our previous work identified key differences in the response to irradiation and *Atm* loss between the neoplastic and vascular compartments within primary mouse tumors(12). To distinguish compartment-specific changes in gene expression, such as vascular and immune cells in specific regions of the tumor and nontumor brain, we needed to profile expression changes at single-cell resolution and in a spatially resolved manner. To achieve such a resolution, we used the 10xGenomics Xenium ISS platform to profile primary p53-null/H3.3K27M mouse DMGs. We examined DMG-bearing mice treated with or without focal brain irradiation (10 Gy x 3), with or without tumor *Atm* loss as depicted in Figure 2A. We examined 5 µm mid-sagittal sections of formalin-fixed, paraffin-embedded (FFPE) tumor-bearing brains. We supplemented 10xGenomics' standard mouse brain content with a custom panel containing padlock probes resulting in 298 brain- and DMG-specific mRNA transcript assays (Supplemental Table 1). Individual cells were detected by nuclear DAPI staining and cell boundaries defined by *in silico* segmentation

(see Methods). This yielded 790,374 individual cells across the four tumor-bearing brains. Next, we clustered cells based on their transcriptional profiles and compared cell type composition between the samples. Uniform Manifold Approximation and Projection (UMAP)(21) reduction, projection, and harmony integration of differentiated normal and neoplastic brain cells into 20 and 29 clusters per specimen, respectively (Figure 2B and Supplemental Figure 3). Examination of differentially expressed marker genes in each cluster identified neoplastic and normal cells including GABAergic interneurons marked by *Gad1* and *Gad2*; microglia marked by *P2ry12*, *Lyz2* and *C1qa*; and endothelial cells marked by *Cd34*, *Fn1*, and *Adgrl4* (Supplemental Figure 4). We used canonical cell-type markers and label transfer-based methods to collapse cell clusters into 10 cell archetypes (neoplastic, endothelial, neuron, astrocyte, oligodendrocyte, microglia, T-lymphocyte, etc.) that could be directly compared across specimens (Supplemental Table 2 and Supplemental Figure 5). This analysis revealed masslike tumors with infiltrating edges recapitulating diffuse glioma biology (Figure 2C). Notably, an *Atm*-null post-irradiation tumor was smaller and involuted, which is suggestive of rapid treatment response. The tumor core, periphery, and nontumor areas were contoured using these data to allow comparisons between matching cell types and locations after irradiation or *Atm* loss (Figure 2C).

We used the spatially resolved expression data to identify differentially expressed genes among neoplastic cells within the tumor cores. We first localized the tumor core within the full-brain sagittal sections using canonical DMG neoplastic cell markers, *Olig1*, *Olig2*, and *Pdgfra* (Figure 3A). As expected, we could not detect *p53* in the neoplastic

cells within the tumor core in the $Tp53^{FL/FL}$ model, whereas low baseline levels could be detected in non-neoplastic cell types (Figure 3B). Similarly, *Atm* transcripts were nearly undetectable in neoplastic cells from *Atm*-null tumor (mean fold-change -0.636, $P < 0.0001$ when compared to *Atm*-intact tumor (Supplemental Figure 6). To identify transcripts that may be differentially expressed after irradiation and/or *Atm* loss, we interrogated differentially expressed genes in neoplastic cells after focal brain irradiation within *Atm* intact tumors (Supplemental Table 3) and *Atm*-null tumors (Supplemental Table 4). *Cyclin-dependent kinase 1a* (*Cdkn1a*), which encodes p21 a potent regulator of cell cycle progression at G1, was the most differentially expressed gene after focal brain irradiation among *Atm* intact tumors (log-fold change 0.8, P-value = 0 by Wilcoxon test, Figure 3C). *Cdkn1a* was still upregulated, albeit to a lesser degree, after focal brain irradiation among *Atm*-null tumors (log-fold change 0.6, P-value = $5.46E-08$ by Wilcoxon test, Figure 3D). Conversely, transcription factors associated with developmental cell states such as *Sox8* and *Sox9* were substantially downregulated after irradiation in *Atm*-intact tumors, while *Sox2*, *Sox4*, *Pdgfra*, and *Olig2* associated with early glial differentiation were all substantially downregulated after irradiation in *Atm*-null tumors. These results identify the differential expression of cell cycle regulators and cell-fate-regulating transcription factors after irradiation in a primary DMG mouse model.

Irradiation and *Atm* loss were associated with changes in the expression of Semaphorin genes specifically, *Semaphorin 6A* (*Sema6a*) and *Semaphorin 3D* (*Sema3d*) which have been implicated in the proliferation and survival of glioma mouse models and glioblastomas(22, 23). After irradiation in *Atm*-intact tumors, *Sema3d* was significantly

increased (log-fold change 1.13, P-value = 0) suggesting that radiation therapy may influence proliferation within the neoplastic core. After irradiation of *Atm*-null tumors, *Sema6a* was significantly decreased (log-fold change -0.40, P-value = 6.59E-15). We utilized snRNA sequencing data from additional primary murine models derived via in utero electroporation approaches to validate Semaphorin, p21, and endothelial interactions in orthogonal models (Supplemental Figure 7) (24). However, our single cell spatial transcriptomics provide additional mechanistic insight indicating that specific Semaphorin genes are altered in neoplastic cells after radiotherapy that might play a critical role in glioma biology.

Neighborhood analysis shows altered immune-neoplastic interactions after treatment.

Targeting ATM combined with irradiation can bridge innate with adaptive immune processes in extracranial cancers (25, 26). This led us to interrogate the spatial relationship between neoplastic cells and immune microenvironment. We examined whether the proximity between neoplastic cells and normal cells varied across irradiated or *Atm*-null tumors. Neighborhood analysis quantified the spatial proximity between different cell types and was used to estimate the mean distance between the neoplastic cells and other cell types (Supplemental Figure 8). These data identified increased proximity of neoplastic cells and immune cells, such as antigen presenting cells and microglia, after *Atm* loss and after treatment with irradiation, which was especially pronounced in the irradiated *Atm*-null tumor. Co-localization analysis between neoplastic cells and other cell types confirmed that microglia and antigen-presenting

cells were most enriched within 0-500 μ m (Figure 3E-H), and these cell types were most co-localized in the irradiated, *Atm*-null tumor (Figure 3H).

Ligand-receptor analysis reveals endothelial cell communications.

Next, cell:cell and cell:ligand receptor interactions in primary mouse DMGs established that endothelial cells had the highest frequency of interactions (Supplemental Figure 9 and Supplemental Table 5). We evaluated statistically significant ligand-receptor interactions (p-value <0.05) among the tumors and identified the interaction between the endothelium, microglia, and neoplastic cells with the Col1a2:CD93 receptor decreased after *Atm* loss and irradiation (Supplemental Figure 9). CD93 plays a role in tumor-associated vasculature (27) and changes in Col1a2 expression has been observed after radiotherapy in other cancers (28). These results provide insight into the changes in endothelial cell interactions after tumor irradiation. After irradiation of *Atm*-intact tumors, the cell:ligand interaction of Sema3a:NRP2 between neoplastic cell and microglia decreased. This interaction has been noted to affect glioma cell migration(29) implying a potential alteration in migration with irradiation. The opposite effect was observed in *Atm*-null tumors after irradiation (Supplemental Figure 9). Thus, ligand-receptor analysis of ISS data suggests that glioma-linked collagen and Semaphorin interactions can be examined in primary DMG mouse models.

Pharmacologic ATM inhibition deregulates DNA damage responses and improves survival. To validate these findings, we confirmed that pharmacological inhibition of ATM could radiosensitize human patient-derived models of DMG. To do so, we tested

whether the brain-penetrant ATM inhibitor AZD1390 (30) combined with focal brain irradiation could similarly improve the survival of a patient-derived xenograft model of H3.3K27M-mutant and p53-mutant diffuse midline glioma, SF8628 (31-34) which lacks a functional ATM mutation (Supplemental Figure 10 and Supplemental Table 6). The combination of AZD1390 and irradiation significantly extended the median survival compared with either treatment alone (Figure 4A). We tested an Atm-intact genetically engineered model with a combination of AZD1930 and irradiation which led to a trend for extended median survival compared to irradiation alone (median 29 days vs. 10 days, p-value = 0.1, Log-rank test, Supplemental Figure 11). These results confirmed that pharmacologic or genetic targeting of ATM can radiosensitize multiple types of *in vivo* DMG models.

We investigated DNA damage response in the SF8628 line by performing western blots in cells treated with AZD1390 with or without irradiation which showed increased expression of GH2AX up to 24 hours post irradiation (Figure 4B and Supplemental Figure 12). To further interrogate effects of irradiation after treatment with AZD1390, we treated Nestin-Tva Cre p53^{F1/F1} PDGF-B H3.3K27M mice (13) with vehicle or drug along with 10 Gy irradiation and harvested mouse brain tumors an hour post irradiation. AZD1390 effectively inhibited ATM as indicated by significantly reduced phospho-KAP1 expression in the treated group when compared to control (p-value 0.01, Mann-Whitney) and increased GH2AX expression (p-value 0.03, Mann-Whitney) in tumor-bearing mice (Figure 4C-F). The differential change in GH2AX in tumor bearing mice

treated with AZD1390 when compared to radiation therapy alone indicates a synergistic effect.

***Atm* radiosensitizes *Cdkn1a*-null primary murine DMGs.**

Next, we dissected the specific functions of p53 that may affect the radiosensitivity of mouse DMG. Our primary models of DMG indicated that the presence of functional p53 is a key determinant of whether tumors are radiosensitized by *Atm* loss. For instance, primary p53-null/H3.3K27M tumors and primary p53-null/*H3f3a*-wildtype tumors were radiosensitized by *Atm* loss (Figure 1E and Deland *et al.* (5), respectively). Conversely, p53 wildtype primary DMG models driven by Ink4A/ARF or PTEN loss are not radiosensitized by *Atm* loss (5, 11). However, it is unknown whether the loss of p53 transcriptional activation and/or loss of other p53 functions enables radiosensitization by *Atm* loss. Our ISS data identified increased *Cdkn1a* expression in neoplastic cells after radiation. Since *Cdkn1a* (encoding p21) is a major transcriptional target of p53 (35), we hypothesized that the loss of *Cdkn1a* function downstream of p53 may be a key determinant of whether *Atm* loss can radiosensitize primary DMGs. To test whether *Cdkn1a* loss allows primary mouse DMGs to be radiosensitized by *Atm* loss, we examined our model of p53-wildtype DMGs driven by Ink4A/ARF loss, which was not radiosensitized by *Atm* loss (Nestin^{TVA}; Ink4A/ARF^{FL/FL}) (5). To test whether p21 loss could radiosensitize these mice when *Atm* was lost, we bred mice with constitutive p21 loss into this genotype (Nestin^{TVA}; p21^{-/-}; Ink4A/ARF^{FL/FL}; *Atm*^{FL/FL} (nlp21A^{FL/FL}). We tested the effects of tumor-specific *Atm* loss by comparing these mice with their littermate controls with intact *Atm* with genotype Nestin^{TVA}; p21^{-/-}; Ink4A/ARF^{FL/FL};

Atm^{FL/FL} (nlp21A^{FL/+}) (Figure 5A). The time to tumor formation was similar regardless of the presence of intact *Atm* (Figure 5B). Surprisingly, p21-null mice bearing tumors with *Atm* deletion had shorter survival following fractionated focal brain irradiation compared to littermate controls with intact *Atm* in the tumors (Figure 5C, P<0.03, log-rank test). We confirmed p21 loss using IHC (Figure 5D-E). p21-null tumors with and without *Atm* loss had similar proliferation indices as assessed by Ki67 staining (Figure 5F). TUNEL staining of irradiated tumors showed that *Atm* loss was associated with significantly increased TUNEL staining (P < 0.05, Figure 5G-H), suggesting that tumors lacking both *Atm* and *Cdkn1a* were primed for apoptosis. These results show that functional *Cdkn1a* is not a key mediator of radiosensitization by *Atm* loss in primary mouse model of DMG.

A p53 transactivation domain mutant retains tumor suppressor function in mouse DMG.

Since *Atm* loss could not radiosensitize *Cdkn1a*-null DMGs, we reasoned that regulation of p53 transcriptional targets other than *Cdkn1a* may cause radioresistance in p53 wild type, *Atm*-null DMGs. To investigate this possibility, we leveraged the conditional *loxP-Stop-loxP-p53*^{25,26} allele (p53^{LSL-25,26}) (36). In the presence of Cre recombinase, this allele expresses p53^{25,26}, a p53 mutant that is severely compromised for the transactivation of most p53 target genes and cannot induce G1-arrest or apoptosis in response to acute DNA damage (36). Interestingly, p53^{25,26} retains tumor suppressor activity in lung tumors (36), however it is unknown whether it retains tumor suppressor activity in brain tumors. We first determined if p53^{25,26} retained tumor suppressor activity in DMG. To test this hypothesis, we compared littermate mice with either p53^{LSL-25,26/FL}

or p53^{FL/FL}. All mice harbored Nestin^{TVA} and were injected with Cre, luciferase, and PDGF-B retrovirus constructs as described above (Figure 6A). We noted a marked delay in tumor presentation in the p53^{LSL-25,26/FL} group compared to that in the p53^{FL/FL} controls (Figure 6B-C). Immunohistochemical analysis revealed heterogeneous p53 expression in the p53^{LSL-25,26/FL} group and apparently absent p53 expression in the p53^{FL/FL} group (Figure 6D-E). Thus, a p53 mutant with severely compromised transactivation activity retains its tumor suppressor activity in primary mouse brainstem gliomas. These results indicate that p53 transactivation function is dispensable for p53 tumor suppression in DMG.

***Atm* loss does not radiosensitize mouse DMGs lacking a functional p53 transactivation domain.**

We next sought to determine if *Atm* loss could radiosensitize DMGs lacking p53 transcriptional activity but retaining other non-transcriptional functions of p53. We previously showed that *Atm* loss did not radiosensitize brainstem gliomas driven by Ink4A/ARF loss, however *Atm* loss modestly radiosensitized brainstem gliomas with both Ink4A/ARF loss and p53 loss (5). We reasoned that if loss of p53 transactivation domain function is the determinant of radiosensitization by *Atm* loss, then brainstem gliomas with both Ink4A/ARF loss and expression of a transactivation-deficient p53^{25,26} allele would be radiosensitized by *Atm* loss. To test if mouse DMGs with p53^{25,26} and Ink4A/ARF loss were radiosensitized by *Atm* loss, we bred mice of genotype Nestin^{TVA}; p53^{LSL-25,26/FL}; Ink4A/ARF^{FL/FL}; *Atm*^{FL/FL}. To test the effects of *Atm* loss, we compared these to littermate controls with the same genotype except an intact *Atm* allele

(Nestin^{TVA}; p53^{LSL-25,26/FL}; Ink4A/ARF^{FL/FL}; Atm^{FL/+}) (Figure 7A). We noted similar time to tumor formation in both models (Figure 7D). *Atm* loss was associated with differential staining of phospho-ATM and phospho-KAP1 after focal brain irradiation (Figure 7B and 7C), confirming the loss of ATM functional activity. After subjecting the mice to fractionated focal brain irradiation, no difference in overall survival was appreciated (Figure 7E). These results indicate that the transactivation-independent functions of p53 may be the primary determinants of whether mouse DMGs can be radiosensitized by *Atm* loss.

Discussion

Here, we describe the generation of primary mouse DMGs based on recent advances in murine genetic engineering including the conditional H3.3K27M allele and the RCAS/tv-a retrovirus platform (10, 13, 14). We used this model to show that the genetic loss of *Atm*, an important target for drugs that have entered clinical trials for brain tumor patients(18), radiosensitizes primary DMG models. Our results in p53-null/H3.3K27M mouse DMGs were similar to those reported previously for p53-null mouse brainstem gliomas(5), in which the sole difference is the presence of H3.3K27M expression from the endogenous *H3f3a* locus in the neoplastic tumor cells in our current model. In addition, we generated several unique genetically engineered mouse models with differential responses based on genotype highlighted in Table 1 which suggests that H3.3K27M is not a primary determinant of the ability to target ATM to enhance the efficacy of radiation therapy in primary mouse DMG models (Supplemental Figure 13).

Our results from genetic experiments in primary mouse models indicate that p53 is a key determinant of the ability of DMG to be radiosensitized by *Atm* loss. Almost all p53-altered primary mouse models were radioresistant and radiosensitized by *Atm* loss, including (i) a model driven by p53 loss with wild type *H3f3a* (5), (ii) a model driven by both p53 loss and loss of *Ink4A/ARF*(5), and (iii) the H3.3K27M/TP53 mutant model reported here (Figure 1E). In contrast, *Atm* loss is unable to radiosensitize primary p53-wildtype brainstem glioma mouse models, including models driven by *Ink4A/ARF* loss(5) and models driven by *Pten* loss (11). Notably, a recent study comprehensively

found that pharmacological ATM inhibition radiosensitized both p53-mutant and p53-wild type patient-derived models of DMG and pediatric high-grade glioma(6)Also, H3.3K27M may enhance ATM signaling, increasing radiosensitivity both with and without ATM inhibition (37). Together, these data suggest that mutational status of p53, H3.3K27M, and other alterations should be tested in correlative analyses in future clinical trials of ATM inhibitors in patients with DMG.

Our ISS data provide the first high-resolution transcriptional analysis at high gene plexy (~300 gene targets) in a mouse tumor model, which is critical to defining the model's tumor vasculature and neoplastic compartments that play distinct roles in therapeutic response (12). Future work will leverage these data to interrogate tumor immune and vascular microenvironment alterations induced by irradiation and *Atm* loss, which may guide the rational design of combinations between radiation therapy, ATM inhibitors, and therapies targeting the immune system or vasculature.

This work has several limitations. H3.3K27M did not decrease tumor latency in our system as has been observed in other experimental systems (38). This may be due to the highly restricted manner of H3.3K27M induction in our system (ie, from the endogeneous *H3f3a* locus and only in spatially- and lineage-restricted cells) and/or the use of a relatively strong PDGFB co-driver alteration that could mask more subtle H3.3K27M driver phenotypes in our system. Also, the presence of an HA tag on both HA-PDGFB and H3.3K27M-Flag-HA constructs precludes specific identification of PDGFB in the nPH system. Finally, we observed a trend for improved overall survival

478 with ATM inhibition in an *Atm*-intact genetic model. We hypothesize that the
479 heterogeneity in tumor latency and timing of treatment delivery may have made a
480 significant survival benefit difficult to detect compared to the genetic loss of *Atm* and
481 compared to the pharmacological xenograft experiment. Future studies could
482 interrogate ATM inhibition effects in *Atm*-null models to dissect on-target from off-target
483 effects of the ATM inhibitor.

484

485

Conclusion

The current work implicates transactivation-independent mechanisms by which p53 mediates radioresistance in *Atm*-null tumors. Our ISS data showed that irradiation elicited overexpression of *Cdkn1a*, a key downstream target of p53 that mediates cell senescence and G1-to-S checkpoint arrest, in p53-null tumors suggesting p53-independent mechanisms of *Cdkn1a* expression (39). This finding led us to dissect the contribution of p53 transactivation functions which regulate p21 expression to radiosensitization in *Atm*-null DMGs. While *Atm* loss radiosensitizes tumors lacking p53, we found that *Atm* loss could not radiosensitize tumors containing a p53^{25,26} allele deficient in p53 transactivation function. Similarly, tumors lacking *Cdkn1a* (p21) could not be radiosensitized by *Atm* loss. Our findings highlight the importance of carefully considering p21 status in clinical trials involving *Atm* inhibition given the complex role of p21 in tumor growth and the microenvironment (40). Strikingly, we found that *Atm* loss made tumors more radioresistant in mice that lacked *Cdkn1a*, and that this finding was associated with increased apoptosis. These findings implicate the transactivation-independent function of p53 as a key determinant of radiosensitivity in *Atm*-null tumors. Future work will dissect the transactivation-independent functions of p53 such as promoting apoptosis through mitochondrial membrane permeabilization, direct repression of transcription, and/or direct interaction with complexes that detect DNA lesions (41, 42). Our data provides genetic and mechanistic insight that builds upon studies of pharmacological ATM inhibition in patient derived xenograft models (6). In addition, our work identifies ATM inhibition improving response to irradiation leading to

509 extended survival. Further studies are needed to determine the transactivation-
510 independent mechanisms of p53 and ATM-directed therapies and their impact on
511 overcoming resistance to radiation therapy in patients with H3.3K27M-mutant DMG.
512

Methods

Detailed workflows for the generation, brain irradiation, and molecular analysis of primary mouse DMG models using RCAS/tv-a and Cre/loxP technologies are found in our recent manuscript(43). Male and female mice were utilized for all murine models. All new reagents, materials, and software are listed in the key resources table (Table 2) . A list of abbreviations utilized is listed in Supplemental table 7.

Sex as a biological variant

Male and female mice were utilized in all murine experiments in this publication to ensure representation of both sexes. We did not identify any sex specific differences in the data, and all findings were consistent across male and female mice. As such, sex was not considered to be a biological variable in the interpretation of the results. The outcomes of this study are therefore expected to be broadly relevant to both sexes.

Mouse strains.

Detailed workflows for generation, brain irradiation, and molecular analysis of primary mouse DMG models using RCAS/tv-a and Cre/loxP technologies are found in our recent *STAR Protocols* manuscript(43). Complex mouse strains were generated by breeding mice with the following alleles: Nes^{TVA}, Atm^{FL}, and p53^{FL} (43), Ink4A/ARF^{FL} (43), the p53^{LSL(25,26)} (36), and the p21^{-/-} (44). The H3f3a^{LSL-K27M-Tag} allele is a gift from Dr. Suzanne Baker(10).

DF1 cell culture and retrovirus generation.

DF1 cells were cultured in Dulbecco's Modified Eagle's medium (DMEM) containing 10% fetal bovine serum (FBS) and RCAS/tv-a retroviruses were generated using RCAS-Cre, RCAS-luc, and RCAS-PDGFB plasmids as previously described(43).

Mouse brainstem injection.

The harvested DF1 cells were injected into the brainstems of mice anesthetized on ice on postnatal day 3-5 as previously described(43). All institutional approvals were obtained prior to the injection. Patient-derived xenografts using the SF8628 model were generated by brainstem injection as described(31-33).

Mouse *in-vivo* imaging

Bioluminescence imaging of gliomas within mice was performed by intraperitoneal injection of D-luciferin and IVIS Illumina III as previously described(43).

Image Guided focal brain irradiation. Irradiation to gliomas within mice was delivered on a Small Animal Radiation Research Platform (SARRP) using image-guided, opposed-lateral beams as described(43). 10 Gy times three consecutive daily fractions was delivered for primary DMG models. 2 Gy times three days a week to 12 Gy total was delivered for patient-derived xenograft DMG models.

ATM inhibitor studies.

Patient-derived xenograft model: SF8628 (H3.3K27M DIPG) was obtained from the University of California San Francisco (UCSF) Medical Center, in accordance with an

557 institutionally approved protocol. Establishment of SF8628 cell culture from surgical
558 specimens, and tumor cell modification for expression of firefly luciferase for in vivo
559 bioluminescence imaging, have been described(31-33). SF8628 cells were propagated
560 as monolayers in complete medium consisting of DMEM supplemented with 10% FBS
561 and non-essential amino acids. Short tandem repeats (STR) were obtained to confirm
562 the identity of cell lines. All cells were cultured in an incubator at 37°C in a humidified
563 atmosphere containing 95% O₂ and 5% CO₂ and were mycoplasma-free at the time of
564 testing. Six-week-old female athymic mice (rnu/rnu genotype, BALB/c background) were
565 purchased from Envigo and housed under aseptic conditions. Pontine injection of tumor
566 cells was performed as previously described (31-33). Each mouse was injected with 1
567 μ L of the SF8628 cell suspension (100,000 cells/ μ L) into the pontine tegmentum at a
568 depth of 5 mm from the inner base of the skull. For the efficacy study of AZD1390 and
569 radiation, animals were randomized into four treatment groups: 1) vehicle control (0.5%
570 hydroxymethylcellulose, 0.1% Tween 80, n=6), 2) ADZ1390 monotherapy (oral gavage
571 of 20 mg/kg of AZD1390 for 5 times a week for two consecutive weeks, n=6), 3)
572 radiation monotherapy (2.0 Gy, 3 times a week for two consecutive weeks for a total
573 dose of 12 Gy, n=6), and 4) AZD1390 and radiation combination therapy
574 (n=6). Biweekly bioluminescence imaging was used to monitor tumor growth and
575 response to therapy as previously described(31). Mice were monitored daily and
576 euthanized at the endpoint which included irreversible neurological deficit or a body
577 condition score of less than 2. Genetically Engineered mouse model: Gliomas were
578 generated using the RCAS/Tv-a system as previously described (45, 46). DF1 Cells
579 were transfected with RCAS plasmids (RCAS-PDGF-B, RCAS-Luc , RCAS-Cre and

mixed in 1:1:1 ratio prior to intracranial injections. nP mice were intracranially injected with 1.0 µl of RCAS virus producing DF1 cells at postnatal day 3 to 5 (P3-P5) and monitored 3x weekly post-weaning for signs of brain tumor symptoms (enlarged head, ataxia, weight loss up to 20%). Bioluminescence imaging was then used to monitor tumor formation from weeks 4-12 as described previously (39). Following tumor detection via imaging or the onset of neurological symptoms, mice were randomized 1:1 into two treatment groups: 1) RT alone or 2) AZD1390 + RT. AZD1390 was obtained from AstraZeneca and resuspended in 0.5% w/v HPMC and 0.1% w/v Tween-80 solution. Mice in the AZD1390 + RT group were dosed at 20 mg/kg via oral gavage one hour prior to RT, as suggested by the superior efficacy dose (18). Both treatment groups received three consecutive daily fractions of 10 Gy of focal brain irradiation delivered by the SARRP. Treated mice were monitored for survival until they reached the humane endpoint. (14, 18)

Immunohistochemistry (IHC)

IHC was performed using methods previously described for Ki67, p-Atm, p-KAP1, total KAP1, γH2AX, and p53(18, 43). Additional IHC and TUNEL staining were performed by HistoWiz Inc. (histowiz.com) using a Standard Operating Procedure and a fully automated workflow for p21 (Cdkn1a), FLAG, and TUNEL on a Bond Rx autostainer (Leica Biosystems) with enzyme treatment (1:1000) using standard protocols. Hematoxylin and eosin (H&E) staining was performed using standard protocols.

Quantification and Statistical Analysis

Statistical significance in volcano plots across ROIs was assessed with the Wilcoxon test on SCTransform normalized count data using the FindMarkers Seurat function. Data plotting and quantification analyses were performed using GraphPad Prism 9. The unpaired t-test was utilized to determine significance in quantification by IHC. The log-rank test was used to determine the survival rate. The Wilcoxon test was used to determine differences in the time to tumor detection. Individual data points were plotted, and all statistically significant values (p value less than 0.05) are identified with an asterisk (*).

Xenium In Situ and Bioinformatics Analysis

Tumor-bearing brains subjected to Xenium ISS were detected by *in vivo* imaging 37-48 days after birth and collected seven days after tumor detection, either after three daily treatments of 10 Gy initiated within two days of tumor detection, or mock treatment. Initial data generated by the Xenium instrument(47) are processed on board with a built-in analysis tool called Xenium Analyzer(47). The Xenium Analyzer is fully automated and includes an imager (imageable area of approximately 12 x 24 mm per slide), sample handling, liquid handling, wide-field epifluorescence imaging, capacity for two slides per run, and an on-instrument analysis pipeline. The analysis pipeline included image pre-processing, puncta detection, transcript decoding and quality score assignment. The pipeline also performed cell segmentation using DAPI images to detect nuclei using a neural network. Each nucleus is then expanded outwards until either a maximum distance of 15 μ m is reached or the boundary of another cell is reached. A variety of output files were produced using an on-instrument pipeline. The

essential files for downstream analysis include the feature-cell matrix (HDF5 and MEX formats identical to those output by single cell RNA tools from 10X (Cellranger/Spaceranger), the transcripts (listing each mRNA, its 3D coordinates, and a quality score), and the cell boundaries CSV file.

Xenium output was first imported into R (4.3.1) using the LoadXenium function from Seurat (4.9.9.9050)(48). The four Xenium samples were processed using Seurat(49). Data was loaded and filtered using `nFeature_Xenium>5` and `nCount_Xenium >10` as criteria. Cells without a predicted annotation were then subset out, and the four samples were normalized using SCTransform. PCA was also run for each sample. There four samples were then integrated using the IntegrateLayers function, using HarmonyIntegration as the method(50).

Specific regions of the tissue were annotated manually using the polygon tool in Xenium Explorer software (development version, 10x Genomics), and the polygon coordinates were exported as csv files. Cells with zero counts were then filtered, and the points within the polygon coordinates were identified using the `point.in.polygon` function in the `sp` (2.0.0) R package. Further plots were generated using Seurat, and deconvolution was performed with `spacexr` (2.2.1)(51) using a custom annotated single cell reference from a previous experiment. DGE analysis across ROIs was assessed using the Wilcoxon test on SCTransform normalized count data using the `FindMarkers` Seurat function. Co-occurrence and neighborhood enrichment plots were made using the

Python package Squidpy (1.2.3)(52), and trajectory and cell-cell-interaction analyses were performed using the Python package STLearn (0.4.12) (53).

All the cells on the entire slide were used to determine the different types of cell clusters. All unlabeled cells were removed for Squidpy and STLearn analyses. Co-occurrence and neighborhood enrichment analyses were conducted on all cells within the entire slide. The tumor core and periphery were utilized to identify cell:cell and cell:ligand interactions. Differentially expressed genes were analyzed in the tumor core.

Whole Genome Bisulfite Sequencing and Bioinformatics Analysis

Bisulfite methylation sequencing and data analysis were performed by Novogene. Briefly, K27M mutant (nPH) and matched K27M wildtype (nP) tumor-bearing mice (n = 4 biological replicates per group) were generated as described above, and tumor-bearing brains embedded in FFPE. Tumor regions were identified in the brains on matched H+E slides, and tumor microdissection was performed. Genomic DNA was isolated, spiked with lambda bacteriophage DNA (to serve as an internal negative control), fragmented to 200-400 base pairs, and bisulfite treatment was performed to convert unmethylated cytosines into uracil via deamination. Notably, this process does not alter methylated cytosines, allowing identification of these sites downstream. After methylation sequencing adapter ligation, double strand DNA synthesis, and library size selection, PCR amplification was performed followed by Illumina sequencing. FastQC was used for quality control on the raw reads. Bismark software (version 0.24.0; Krueger et al., 2011) was used to perform alignments of bisulfite-treated reads to a

reference genome (-X 700--dovetail). The reference genome was firstly transformed into bisulfite-converted version (C-to-T and G-to-A converted) and then indexed using bowtie2 (Langmead et al., 2012). Sequence reads were also transformed into fully bisulfite-converted versions (C-to-T and G-to-A converted) before they are aligned to similarly converted versions of the genome in a directional manner. Sequence reads that produce a unique best alignment from the two alignment processes (original top and bottom strand) are then compared to the normal genomic sequence and the methylation state of all cytosine positions in the read is inferred. The same reads that aligned to the same regions of genome were regarded as duplicated ones. The sequencing depth and coverage were summarized using deduplicated reads. The results of methylation extractor (bismark_methylation_extractor,-- no_overlap) were transformed into bigWig format for visualization using IGV browser. The sodium bisulfite non-conversion rate was calculated as the percentage of cytosine sequenced at cytosine reference positions in the lambda genome. Genes were extracted from genome assembly GRCm39 using Ensembl gene set Ver 111. Promoter regions are defined from 1500 bp upstream of TSS to 500 bp downstream. For each region, methylated CpG reads and unmethylated reads were counted, summed and average methylation level was calculated. Similarly, putative enhancers were extracted from Ensembl regulation Ver 111 of GRCm39 and an average methylation level was calculated for each enhancer. Methylation difference was determined for each feature (promoter and enhancer) between samples of K27M group and samples of nPA group. Significance was estimated by applying ANOVA over a linear model fit(54). For DNA methylation extraction we used methkit. Motif analysis was carried out by HOMER which is available

695 online at <http://homer.ucsd.edu/homer>. For pathway enrichment analysis STRING was
696 used. For "other tissues" we analyzed data from GSE42836. methylation extraction
697 using the methkit.
698

699 **Declarations**

700

701 **Study approval**

702

703 All animal studies were approved by the institutional animal protocol. All animal
704 experiments were approved by the Institutional Animal Care and Use Committee at
705 Duke and Northwestern University.

706

707 **Consent for Publication**

708

709 Not applicable

710

711 **Availability of data and materials**

712 All data were deposited in the GEO database. The accession number for the in situ
713 sequencing is GSE246584 and whole genome bisulfite sequencing is GSE284759. This
714 study does not report original code. Additional information required to reanalyze the
715 data reported in this paper is available from the corresponding author upon request. All
716 raw values for figures are available in Supplemental table 8.

717

718 **Competing Interests**

719

720 DGK is a cofounder and stockholder in XRAD Therapeutics, which is developing
721 radiosensitizers. DGK is a member of the scientific advisory board and owns stock in

Lumicell Inc, a company commercializing intraoperative imaging technology. None of these affiliations represent a conflict of interest with respect to the work described in this manuscript. DGK is a coinventor on a patent for a handheld imaging device and is a coinventor on a patent for radiosensitizers. XRAD Therapeutics, Merck, Bristol Myers Squibb, and Varian Medical Systems have provided research support to DGK, but this did not support the research described in this manuscript. ZJR receives royalties for intellectual property related to brain tumor diagnostic tests that is managed by the Duke Office of Licensing and Ventures and has been licensed to Genetron Health, and honoraria for teaching from Oakstone Publishing and Eisai Pharmaceuticals. The other authors have no conflicts of interests to declare.

Funding

We thank sources of funding including NCI K08256045 Mentored Clinician Scientist Development Award, Alex's Lemonade Stand Foundation A Award No. 23-27774, ChadTough Defeat DIPG Foundation, the SoSo Strong Foundation, the Pediatric Brain Tumor Foundation, the Emily Beazley's Kures for Kids Fund, the St. Baldrick's Foundation, Lauren Brescia Memorial Fund, and NCI P50CA190991 Duke SPORE in Brain Cancer developmental funds to ZJR. This work was also supported by 7R35CA197616 from the NCI to DGK. We thank Hyundai Hope on Wheels for funding to OJB.

Author contributions

745
746 AM prepared the manuscript, designed experiments, and analyzed data. VV designed
747 and led the execution of experiments for the revised manuscript including mouse tissue
748 analyses, whole-genome bisulfite sequencing, and pharmacologic in vivo experiments.
749 AM and VV share the first author position. The listed order of the first authors was
750 determined by alphabetical order of the last names. The order was determined to be A-
751 Z based on a coin-flip from the corresponding author ZJR. AM, ZJR, SGG, DGK, DMA
752 and OJB designed the study and experiments. SW, HL, BEF, LW, MEG, DG, LL, KD,
753 VV, SM, MR and ZJR performed mouse experiments and tabulated data. NTW
754 performed mouse irradiations. KA and NH performed patient-derived xenograft and
755 ATM inhibitor pharmacologic experiments. LA contributed p53 transactivation mutant
756 mouse strain and experimental design regarding the strain. EH, KA, LW, and ZJR
757 assisted with in situ sequencing experiments. MA, VJ, JAR, SG and ZJR performed
758 bioinformatic analyses. TM performed whole-genome bisulfite sequencing analyses.
759 AM, ZJR, and SGG prepared the manuscript.

760

761 **Acknowledgements**

762

763 We thank Dr. Suzanne Baker, St Jude Research Hospital, Memphis Tennessee for the
764 gift of the H3f3a-loxP-Stop-loxP-K27M-Tag mice. Funds for ISS data generation were
765 provided by the Duke Brain Tumor Omics Program, Durham, North Carolina.

766

767

References

1. Wu G, Broniscer A, McEachron TA, Lu C, Paugh BS, Becksfort J, et al. Somatic histone H3 alterations in pediatric diffuse intrinsic pontine gliomas and non-brainstem glioblastomas. *Nat Genet.* 2012;44(3):251-3.
2. Schwartzentruber J, Korshunov A, Liu XY, Jones DT, Pfaff E, Jacob K, et al. Driver mutations in histone H3.3 and chromatin remodelling genes in paediatric glioblastoma. *Nature.* 2012;482(7384):226-31.
3. Zhang L, Chen LH, Wan H, Yang R, Wang Z, Feng J, et al. Exome sequencing identifies somatic gain-of-function PPM1D mutations in brainstem gliomas. *Nat Genet.* 2014;46(7):726-30.
4. Werbrouck C, Evangelista CCS, Lobon-Iglesias MJ, Barret E, Le Teuff G, Merlevede J, et al. TP53 Pathway Alterations Drive Radioresistance in Diffuse Intrinsic Pontine Gliomas (DIPG). *Clin Cancer Res.* 2019;25(22):6788-800.
5. Deland K, Starr BF, Mercer JS, Byemerwa J, Crabtree DM, Williams NT, et al. Tumor genotype dictates radiosensitization after Atm deletion in primary brainstem glioma models. *J Clin Invest.* 2021;131(1).
6. Xie J, Kuriakose T, Bianski B, Twarog N, Savage E, Xu K, et al. ATM inhibition enhances the efficacy of radiation across distinct molecular subgroups of pediatric high-grade glioma. *Neuro Oncol.* 2023.
7. Khadka P, Reitman ZJ, Lu S, Buchan G, Gionet G, Dubois F, et al. PPM1D mutations are oncogenic drivers of de novo diffuse midline glioma formation. *Nat Commun.* 2022;13(1):604.
8. du Chatinier A, Meel MH, Das AI, Metselaar DS, Waranecki P, Bugiani M, et al. Generation of immunocompetent syngeneic allograft mouse models for pediatric diffuse midline glioma. *Neurooncol Adv.* 2022;4(1):vdac079.
9. McNicholas M, De Cola A, Bashardanesh Z, Foss A, Lloyd CB, Hebert S, et al. A Compendium of Syngeneic, Transplantable Pediatric High-Grade Glioma Models Reveals Subtype-Specific Therapeutic Vulnerabilities. *Cancer Discov.* 2023.
10. Larson JD, Kasper LH, Paugh BS, Jin H, Wu G, Kwon CH, et al. Histone H3.3 K27M Accelerates Spontaneous Brainstem Glioma and Drives Restricted Changes in Bivalent Gene Expression. *Cancer Cell.* 2019;35(1):140-55 e7.
11. Stewart CE, Guerra-Garcia ME, Luo L, Williams NT, Ma Y, Regal JA, et al. The Effect of Atm Loss on Radiosensitivity of a Primary Mouse Model of Pten-Deleted Brainstem Glioma. *Cancers (Basel).* 2022;14(18).
12. Deland K, Mercer JS, Crabtree DM, Guerra Garcia ME, Reinsvold M, Campos LDS, et al. Radiosensitizing the Vasculature of Primary Brainstem Gliomas Fails to Improve Tumor Response to Radiation Therapy. *Int J Radiat Oncol Biol Phys.* 2022;112(3):771-9.
13. Cordero FJ, Huang Z, Grenier C, He X, Hu G, McLendon RE, et al. Histone H3.3K27M Represses p16 to Accelerate Gliomagenesis in a Murine Model of DIPG. *Mol Cancer Res.* 2017;15(9):1243-54.

14. Hoeman CM, Cordero FJ, Hu G, Misuraca K, Romero MM, Cardona HJ, et al. ACVR1 R206H cooperates with H3.1K27M in promoting diffuse intrinsic pontine glioma pathogenesis. *Nat Commun.* 2019;10(1):1023.
15. Hambardzumyan D, Amankulor NM, Helmy KY, Becher OJ, and Holland EC. Modeling Adult Gliomas Using RCAS/t-va Technology. *Transl Oncol.* 2009;2(2):89-95.
16. Tomita Y, Shimazu Y, Somasundaram A, Tanaka Y, Takata N, Ishi Y, et al. A novel mouse model of diffuse midline glioma initiated in neonatal oligodendrocyte progenitor cells highlights cell-of-origin dependent effects of H3K27M. *Glia.* 2022;70(9):1681-98.
17. Garcia MEG, Kirsch DG, and Reitman ZJ. Targeting the ATM Kinase to Enhance the Efficacy of Radiotherapy and Outcomes for Cancer Patients. *Semin Radiat Oncol.* 2022;32(1):3-14.
18. Durant ST, Zheng L, Wang Y, Chen K, Zhang L, Zhang T, et al. The brain-penetrant clinical ATM inhibitor AZD1390 radiosensitizes and improves survival of preclinical brain tumor models. *Sci Adv.* 2018;4(6):eaat1719.
19. Lewis PW, Muller MM, Koletsky MS, Cordero F, Lin S, Banaszynski LA, et al. Inhibition of PRC2 activity by a gain-of-function H3 mutation found in pediatric glioblastoma. *Science.* 2013;340(6134):857-61.
20. Filbin MG, Tirosh I, Hovestadt V, Shaw ML, Escalante LE, Mathewson ND, et al. Developmental and oncogenic programs in H3K27M gliomas dissected by single-cell RNA-seq. *Science.* 2018;360(6386):331-5.
21. van der Maarten LH, G. Visualizing Data using t-SNE. *Journal of Machine Learning Research.* 2008;9:2579-605
22. Zhao J, Tang H, Zhao H, Che W, Zhang L, and Liang P. SEMA6A is a prognostic biomarker in glioblastoma. *Tumour Biol.* 2015;36(11):8333-40.
23. Angelucci C, Lama G, and Sica G. Multifaceted Functional Role of Semaphorins in Glioblastoma. *Int J Mol Sci.* 2019;20(9).
24. McNicholas M, De Cola A, Bashardanesh Z, Foss A, Lloyd CB, Hébert S, et al. A Compendium of Syngeneic, Transplantable Pediatric High-Grade Glioma Models Reveals Subtype-Specific Therapeutic Vulnerabilities. *Cancer Discov.* 2023;13(7):1592-615.
25. Hu M, Zhou M, Bao X, Pan D, Jiao M, Liu X, et al. ATM inhibition enhances cancer immunotherapy by promoting mtDNA leakage and cGAS/STING activation. *J Clin Invest.* 2021;131(3).
26. Zhang Q, Green MD, Lang X, Lazarus J, Parsels JD, Wei S, et al. Inhibition of ATM Increases Interferon Signaling and Sensitizes Pancreatic Cancer to Immune Checkpoint Blockade Therapy. *Cancer Res.* 2019;79(15):3940-51.
27. Tossetta G, Piani F, Borghi C, and Marzioni D. Role of CD93 in Health and Disease. *Cells.* 2023;12(13).
28. Yao G, Zhao K, Bao K, and Li J. Radiation increases COL1A1, COL3A1, and COL1A2 expression in breast cancer. *Open Med (Wars).* 2022;17(1):329-40.
29. Nasarre C, Koncina E, Labourdette G, Cremel G, Roussel G, Aunis D, et al. Neuropilin-2 acts as a modulator of Sema3A-dependent glioma cell migration. *Cell Adh Migr.* 2009;3(4):383-9.
30. !!! INVALID CITATION !!! (18).

31. Katagi H, Louis N, Unruh D, Sasaki T, He X, Zhang A, et al. Radiosensitization by Histone H3 Demethylase Inhibition in Diffuse Intrinsic Pontine Glioma. *Clin Cancer Res.* 2019;25(18):5572-83.
32. Hashizume R, Andor N, Ihara Y, Lerner R, Gan H, Chen X, et al. Pharmacologic inhibition of histone demethylation as a therapy for pediatric brainstem glioma. *Nat Med.* 2014;20(12):1394-6.
33. Aoki Y, Hashizume R, Ozawa T, Banerjee A, Prados M, James CD, et al. An experimental xenograft mouse model of diffuse pontine glioma designed for therapeutic testing. *J Neurooncol.* 2012;108(1):29-35.
34. Pal S, Kozono D, Yang X, Fendler W, Fitts W, Ni J, et al. Dual HDAC and PI3K Inhibition Abrogates NFκB- and FOXM1-Mediated DNA Damage Response to Radiosensitize Pediatric High-Grade Gliomas. *Cancer Res.* 2018;78(14):4007-21.
35. Brugarolas J, Chandrasekaran C, Gordon JI, Beach D, Jacks T, and Hannon GJ. Radiation-induced cell cycle arrest compromised by p21 deficiency. *Nature.* 1995;377(6549):552-7.
36. Brady CA, Jiang D, Mello SS, Johnson TM, Jarvis LA, Kozak MM, et al. Distinct p53 transcriptional programs dictate acute DNA-damage responses and tumor suppression. *Cell.* 2011;145(4):571-83.
37. Peterson E, Parsels LA, Parsels JD, Zhao X, Castro MG, Lawrence TS, et al. Inhibition of H3K27M-enhanced ATM signaling increases radiation efficacy in diffuse midline glioma. *bioRxiv.* 2024:2024.11.01.621526.
38. !!! INVALID CITATION !!! (10, 16, 38).
39. Galanos P, Vougas K, Walter D, Polyzos A, Maya-Mendoza A, Haagensen EJ, et al. Chronic p53-independent p21 expression causes genomic instability by deregulating replication licensing. *Nat Cell Biol.* 2016;18(7):777-89.
40. Hukkelhoven E, Liu Y, Yeh N, Ciznadija D, Blain SW, and Koff A. Tyrosine phosphorylation of the p21 cyclin-dependent kinase inhibitor facilitates the development of proneural glioma. *J Biol Chem.* 2012;287(46):38523-30.
41. Boutelle AM, and Attardi LD. p53 and Tumor Suppression: It Takes a Network. *Trends Cell Biol.* 2021;31(4):298-310.
42. Ho T, Tan BX, and Lane D. How the Other Half Lives: What p53 Does When It Is Not Being a Transcription Factor. *Int J Mol Sci.* 2019;21(1).
43. Weidenhammer LB, Liu HQ, Luo L, Williams NT, Deland K, Kirsch DG, et al. Inducing primary brainstem gliomas in genetically engineered mice using RCAS/TVA retroviruses and Cre/loxP recombination. *STAR Protocols.* 2023;4(1):102094.
44. Deng C, Zhang P, Harper JW, Elledge SJ, and Leder P. Mice lacking p21CIP1/WAF1 undergo normal development, but are defective in G1 checkpoint control. *Cell.* 1995;82(4):675-84.
45. Misuraca KL, Barton KL, Chung A, Diaz AK, Conway SJ, Corcoran DL, et al. Pax3 expression enhances PDGF-B-induced brainstem gliomagenesis and characterizes a subset of brainstem glioma. *Acta Neuropathol Commun.* 2014;2:134.

46. Misuraca KL, Hu G, Barton KL, Chung A, and Becher OJ. A Novel Mouse Model of Diffuse Intrinsic Pontine Glioma Initiated in Pax3-Expressing Cells. *Neoplasia*. 2016;18(1):60-70.
47. Amanda J, Robert S, Andrew G, Florian W, Morgane R, Ghezal B, et al. High resolution mapping of the breast cancer tumor microenvironment using integrated single cell, spatial and in situ analysis of FFPE tissue. *bioRxiv*. 2022:2022.10.06.510405.
48. Yuhua H, Tim S, Madeline K, Saket C, Paul H, Austin H, et al. Dictionary learning for integrative, multimodal, and scalable single-cell analysis. *bioRxiv*. 2022:2022.02.24.481684.
49. Hao Y, Stuart T, Kowalski MH, Choudhary S, Hoffman P, Hartman A, et al. Dictionary learning for integrative, multimodal and scalable single-cell analysis. *Nature Biotechnology*. 2024;42(2):293-304.
50. Korsunsky I, Millard N, Fan J, Slowikowski K, Zhang F, Wei K, et al. Fast, sensitive and accurate integration of single-cell data with Harmony. *Nature Methods*. 2019;16(12):1289-96.
51. Cable DM, Murray E, Shanmugam V, Zhang S, Zou LS, Diao M, et al. Cell type-specific inference of differential expression in spatial transcriptomics. *Nat Methods*. 2022;19(9):1076-87.
52. Palla G, Spitzer H, Klein M, Fischer D, Schaar AC, Kuemmerle LB, et al. Squidpy: a scalable framework for spatial omics analysis. *Nat Methods*. 2022;19(2):171-8.
53. Duy P, Xiao T, Jun X, Laura FG, Pui Yeng L, Arti R, et al. stLearn: integrating spatial location, tissue morphology and gene expression to find cell types, cell-cell interactions and spatial trajectories within undissociated tissues. *bioRxiv*. 2020:2020.05.31.125658.
54. Falick Michaeli T, Sabag O, Fok R, Azria B, Monin J, Nevo Y, et al. Muscle injury causes long-term changes in stem-cell DNA methylation. *Proceedings of the National Academy of Sciences*. 2022;119(52):e2212306119.

Figure 1

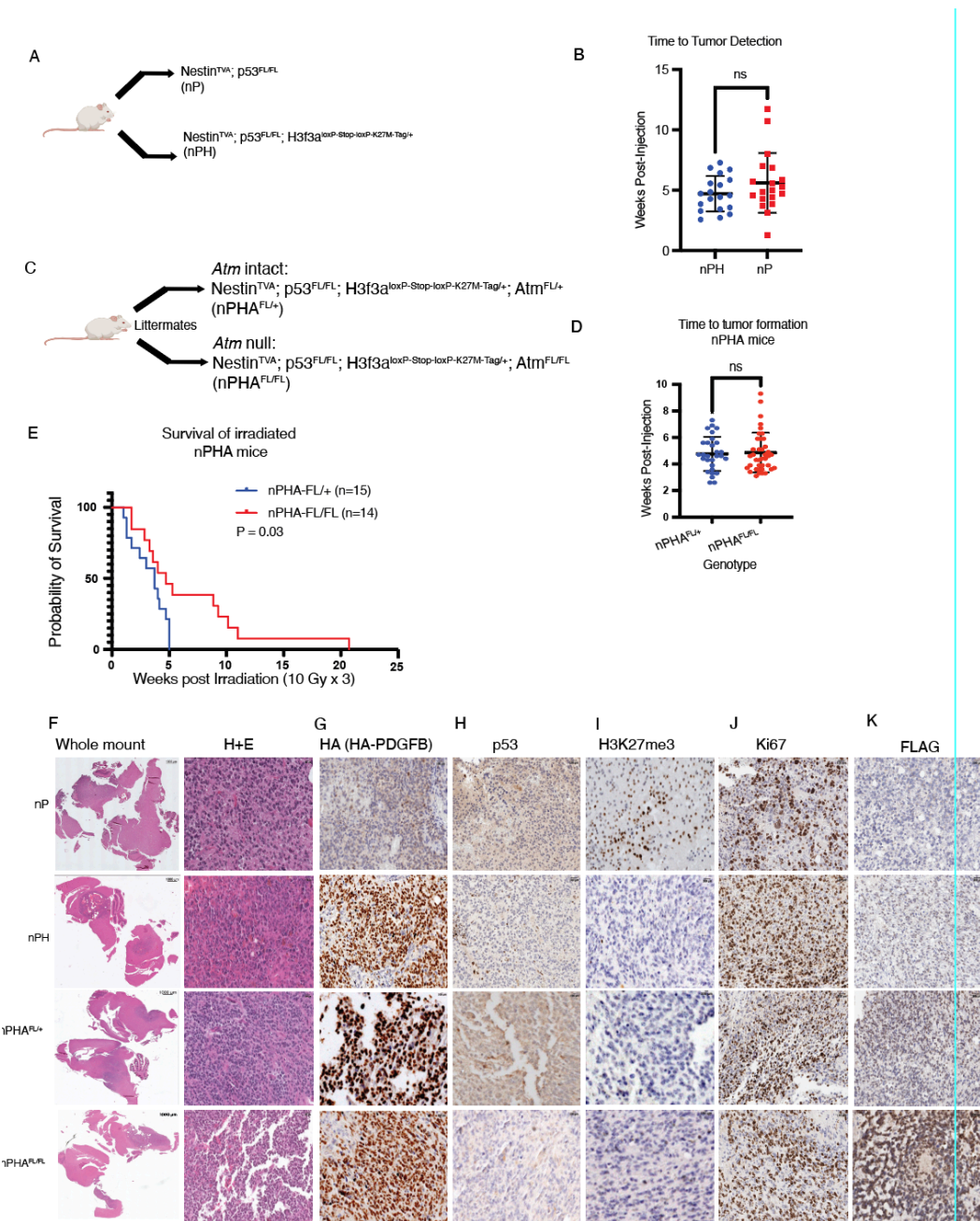


Figure 1. Atm loss improves radiosensitivity of primary murine diffuse midline gliomas generated using a conditional H3.3K27M allele. (A) Representation of mouse genotypes used to generate primary mouse DMGs with p53 loss (Nestin^{TVA};

939 p53^{FL/FL}, nP) and mouse DMGs with p53 loss and H3.3K27M (Nestin^{TVA}; p53^{FL/FL};
940 H3f3a^{loxP-Stop-loxP-K27M-Tag/+}, nPH) with or without conditional H3.3K27M allele. Mice also
941 contained one intact and one floxed allele of Atm (Atm^{FL/+}, not shown).

942 (A) Dot plot showing time to tumor formation between nPH and nP mice
943 without any statistical significance. Statistical test utilized Welch's t-test.

944 (B) Schematic showing nPHA^{FL/+} (Atm^{FL/+}) and nPHA^{FL/FL} (Atm^{FL/FL}) within
945 RCAS/TVA retrovirus and conditional H3K27M allele.

946 (C) Time to tumor formation showing no statistical difference between
947 nPHA^{FL/FL} and nPHA^{FL/+} mice. Statistical test utilized Welch's t-test.

948 (D) Overall survival of between nPHA^{FL/FL} and nPHA^{FL/+} mice following three
949 daily fractions of 10 Gy image-guided focal brain irradiation shows
950 significantly longer median survival in nPHA^{FL/FL} (p-value = 0.03) using
951 Mantel Cox (log rank test).

952 (E) Whole mount and H&E slides showing tumor within nP, nPH, nPHA^{FL/+} and
953 nPHA^{FL/FL} (top to bottom) mice exhibiting hypercellularity and infiltration of
954 normal brain.

955 (F) IHC for HA expression indicating the presence of the PDGF-B HA tag.

956 (G) IHC for p53.

957 (H) IHC for histone 3 lysine 27 trimethylation (H3K27me3).

958 (I) IHC displaying the Ki67 proliferation of tumors.

959 (J) Anti-Flag IHC confirmed the presence of the Flag-HA tag.

960 Scale bar for all H&E and IHC images (C-H) = 50 μ m. Scale bar for Whole Mount
961 = 200 μ m. Scale bar for FLAG IHC infiltrating biology (I) = 500 μ m

Figure 2

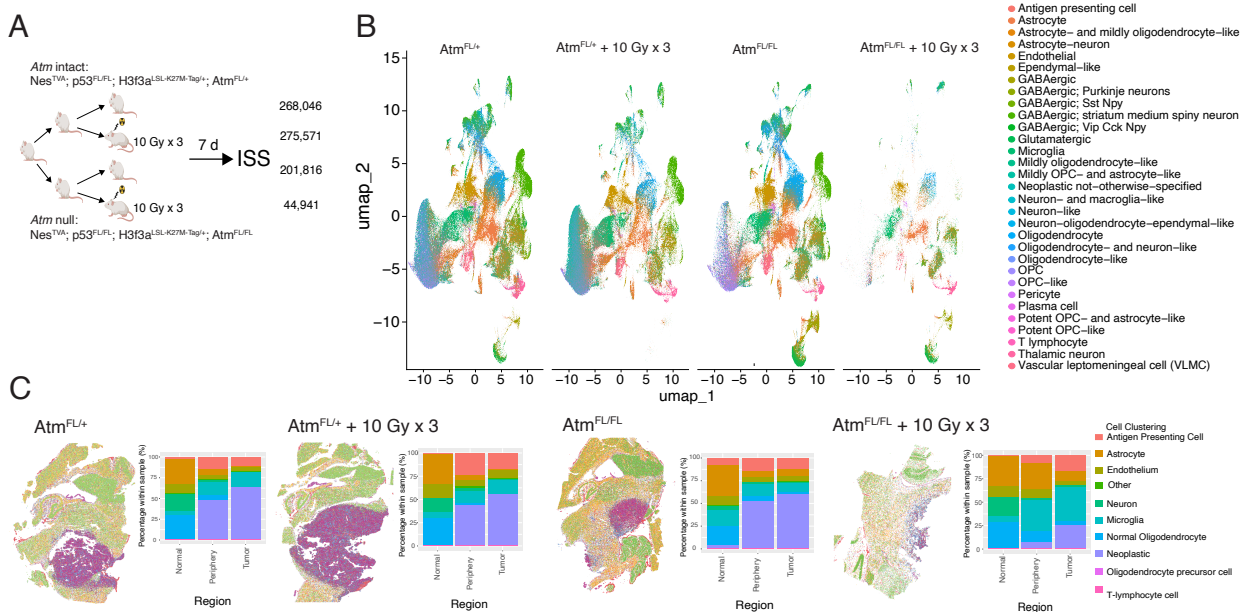


Figure 2. Spatial clustering in primary mouse DMGs treated with focal brain irradiation or tumoral *Atm* deletion.

(A) Schematic of DMG-bearing mice with *Atm* intact or null within the tumors, with and without focal brain irradiation that underwent in situ spatial transcriptomic sequencing (ISS). All mice were Nestin^{TVA}; p53^{FL/FL}; H3f3a^{loxP-Stop-loxP-K27M-Tag/+} with either *Atm* intact (*Atm*^{FL/+}) or *Atm* null (*Atm*^{FL/FL}) in the tumor.

(B) Harmony integration showing clustering of n=4 tumor bearing mice with H3f3a^{loxP-Stop-loxP-K27M-Tag/+} with either *Atm* intact (*Atm*^{FL/+}) or *Atm* null (*Atm*^{FL/FL}) in the tumor.

(C) Spatial clustering of cells into n=10 cell archetypes based on label transfer in n=4 tumor-bearing mouse brains (left), H&E of whole brain (middle),

976 distribution of cells within normal brain, tumor periphery and tumor core
977 annotated in bar graph (*right*). Top row indicates *Atm* intact with and
978 without irradiation. Bottom row indicates *Atm* null with and without
979 irradiation. Color legend to the right corresponds to individual cell type
980 noted on bar graph.

981 (D) Spatial identification of tumors by expression of *Pdgfra*, *Olig1*, and *Olig2*
982 within all conditions: *Atm* intact, *Atm* intact with irradiation, *Atm* null, *Atm*
983 null with irradiation (*top to bottom*).

984 (E) Spatial identification of p53 loss in all tumor conditions: *Atm* intact without
985 and with irradiation (*top row, left to right*). *Atm* null without and with
986 irradiation (*bottom row, left to right*).

987 (F) Key differentially expressed genes in *Atm*-intact neoplastic tumor cells
988 treated with and without focal brain irradiation. Log₂ fold change and p-
989 value for all genes in Table S3.

990 (G) Key differentially expressed genes in *Atm*-null neoplastic tumor cells
991 treated with and without focal brain irradiation. Log₂ fold change and p-
992 value for all genes in Table S4.

993

994 All cells within entire slide were used for distribution of cells identified in Figure 3b.

995 Tumor core and periphery were utilized to identify the key differentially expressed genes

996 (Figure F-G)

997

Figure 3

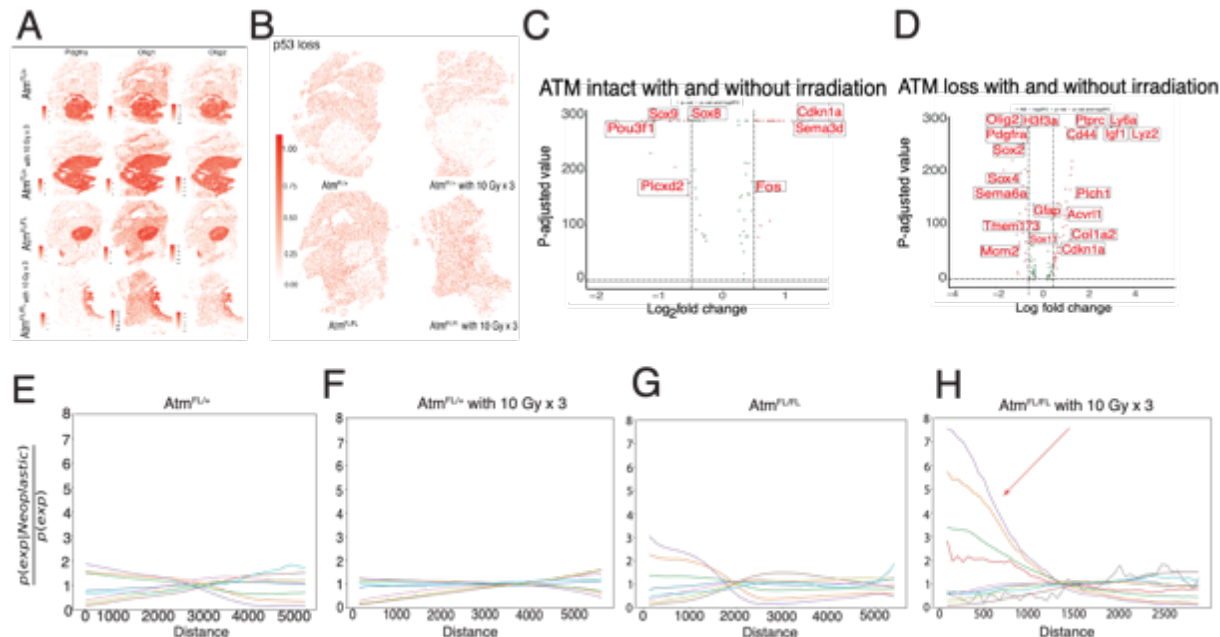


Figure 3. Differentially expressed genes and neighborhood analysis of primary mouse DMGs with tumoral *Atm* loss and/or focal irradiation.

(A) Spatial identification of tumors by expression of *Pdgfra*, *Olig1*, and *Olig2* within all conditions: *Atm* intact, *Atm* intact with irradiation, *Atm* null, *Atm* null with irradiation (top to bottom).

(B) Spatial identification of p53 loss in all tumor conditions: *Atm* intact without and with irradiation (top row, left to right). *Atm* null without and with irradiation (bottom row, left to right).

(C) Key differentially expressed genes in *Atm*-intact neoplastic tumor cells treated with and without focal brain irradiation. Log₂ fold change and p-value for all genes in Table S3.

1011 (D) Key differentially expressed genes in *Atm*-null neoplastic tumor cells
1012 treated with and without focal brain irradiation. Log₂ fold change and p-
1013 value for all genes in Table S4.

1014 (E) Co-occurrence plot of *Atm*-intact (nPHA^{FL/+}) tumor showing number
1015 compared to distance of various cell types in relation to neoplastic cells.

1016 (F) Co-occurrence plot of *Atm*-intact (nPHA^{FL/+}) tumor with irradiation showing
1017 number compared to distance of various cell types in relation to neoplastic
1018 cells.

1019 (G) Co-occurrence plot of *Atm*-null (nPHA^{FL/FL}) tumor showing number
1020 compared to distance of various cell types in relation to neoplastic cells.

1021 (H) Co-occurrence plot of *Atm*-null (nPHA^{FL/FL}) tumor with irradiation showing
1022 number compared to distance of various cell types in relation to neoplastic
1023 cells. Red arrow indicates increased frequency of immune cells compared
1024 to neoplastic cells

1025

1026 Color Legend for Figure (E-H) on right side panel. APC – Antigen Presenting Cell. OPC
1027 – Oligodendrocyte precursor cell. TLC- T Lymphocyte cell. Neighborhood enrichment
1028 and co-occurrence analysis were conducted on entire slide. All unlabeled cells were
1029 removed for analysis.

1030

1031

Figure 4

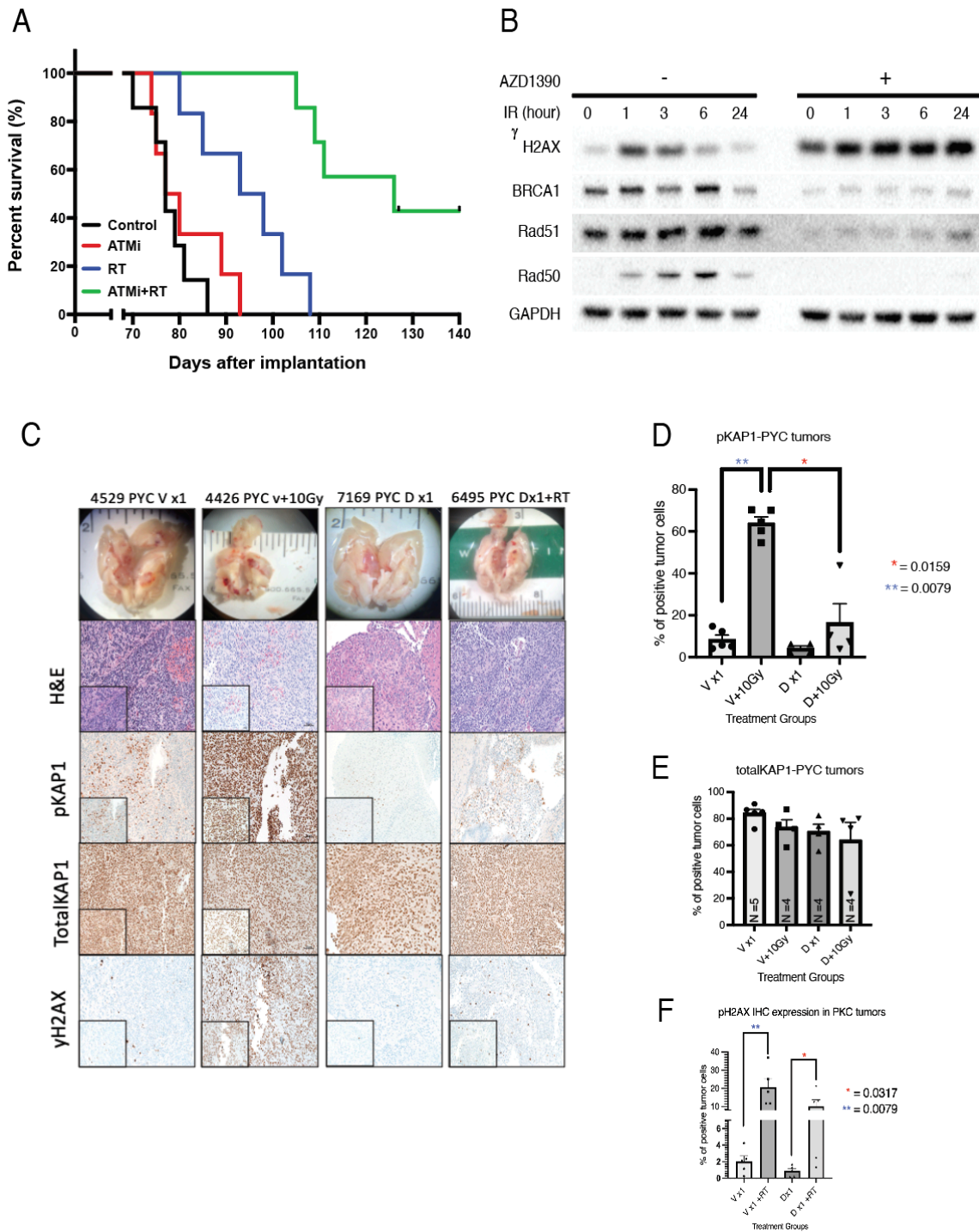


Figure 4. Pharmacologic inhibition and DNA damage response signaling in primary mouse DMGs with tumoral *Atm* loss and/or focal irradiation.

(A) Overall survival of mice bearing SF8628 diffuse midline glioma patient-derived xenografts were treated with 20mg/kg of AZD1390 for 2 weeks (ATMi, 5 days a week x 2 weeks) and/or focal brain irradiation (RT, 2 Gy x 3 days a week for 12 Gy total).

(B) Western blot of SF8628 followed by AZD1390 treatment with and without radiation (0h, 1h, 3h, 6h, 24h)

(C) Representative IHC of Nestin^{TV} p53^{FL/FL} PDGF-B +H3.3K27M +Cre (PKC) treated with vehicle (V) or ATM inhibitor drug (D), AZD1390 with and without irradiation of 10 Gy for the following antibodies (Top to bottom): H&E, pKAP1, total KAP1, γH2AX

(D) PDGF-B +H3.3K27M + p53^{FL/FL} (n=5 per treatment group) stained with phospho-KAP1 demonstrate increased phosphor-KAP1 expression in samples treated with one dose of 10Gy and show significance in vehicle treated samples (PKC + V +/- irradiation (RT)) with a p-value = 0.0079 (Mann-Whitney). This expression is significantly reduced in drug (D) with irradiation (RT) when compared to vehicle (V) with irradiation (RT) samples suggesting ATM inhibitor, AZD 1390 sensitizes the DIPG tumor bearing mice to irradiation (p-value = 0.0159, Mann-Whitney test).

(E) PDGF-B +H3.3K27M + p53^{FL/FL} (n=5 per treatment group) stained with total KAP1 show unchanged levels across all treatment groups.

1057 (F) PDGF-B +H3.3K27M + p53^{FL/FL} (n=5 per treatment group) stained with
1058 γH2AX demonstrates increased expression in samples treated with
1059 irradiation with one dose of 10Gy when compared to their respective non-
1060 RT treated samples (p-value = 0.0079, Mann Whitney test for vehicle
1061 treated groups and p-value = 0.0317, Mann Whitney test for drug treated
1062 groups).

1063 Scale bar = 50uM on IHC

1064

1065

1066

1067

1068

Figure 5

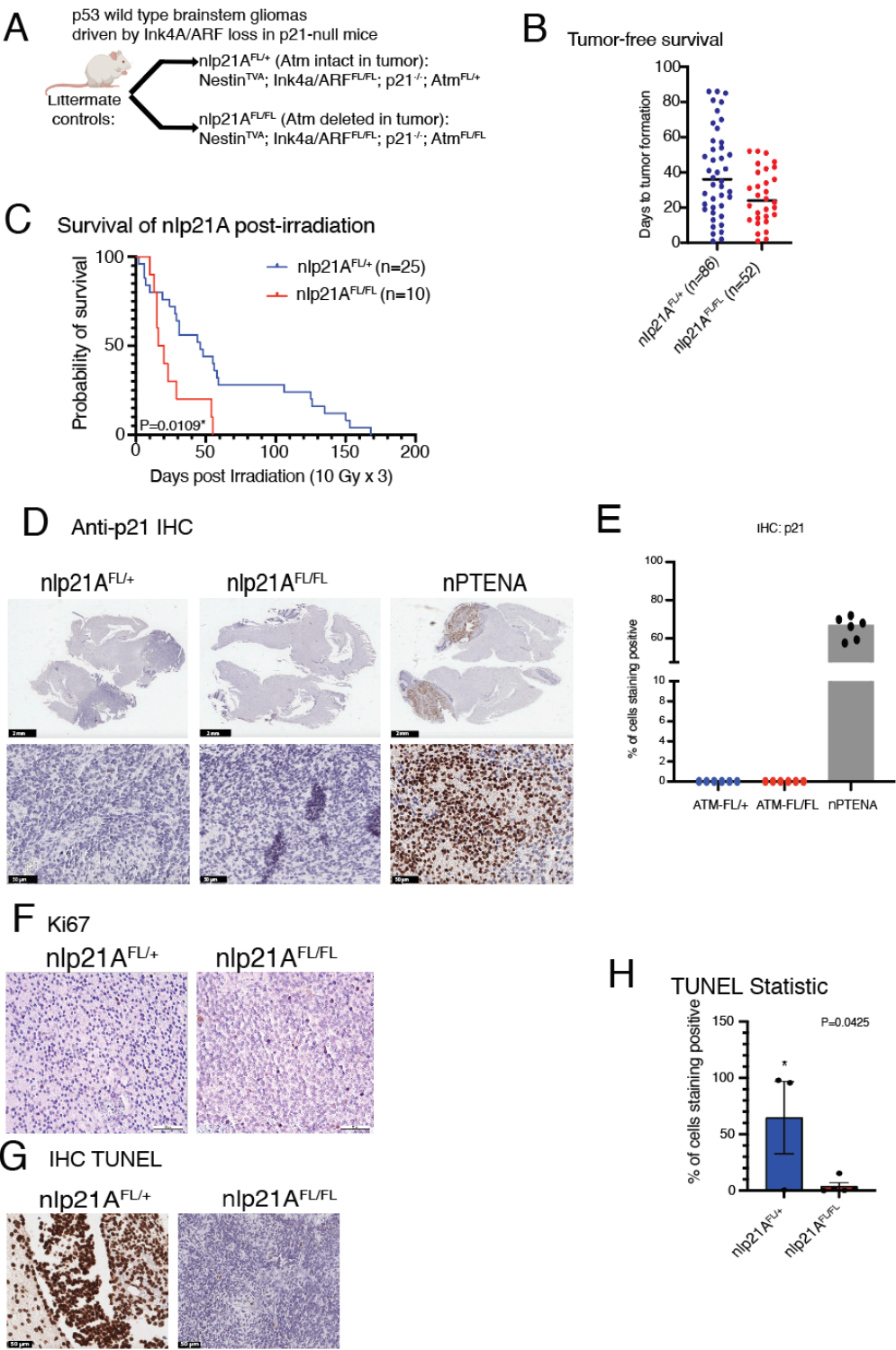
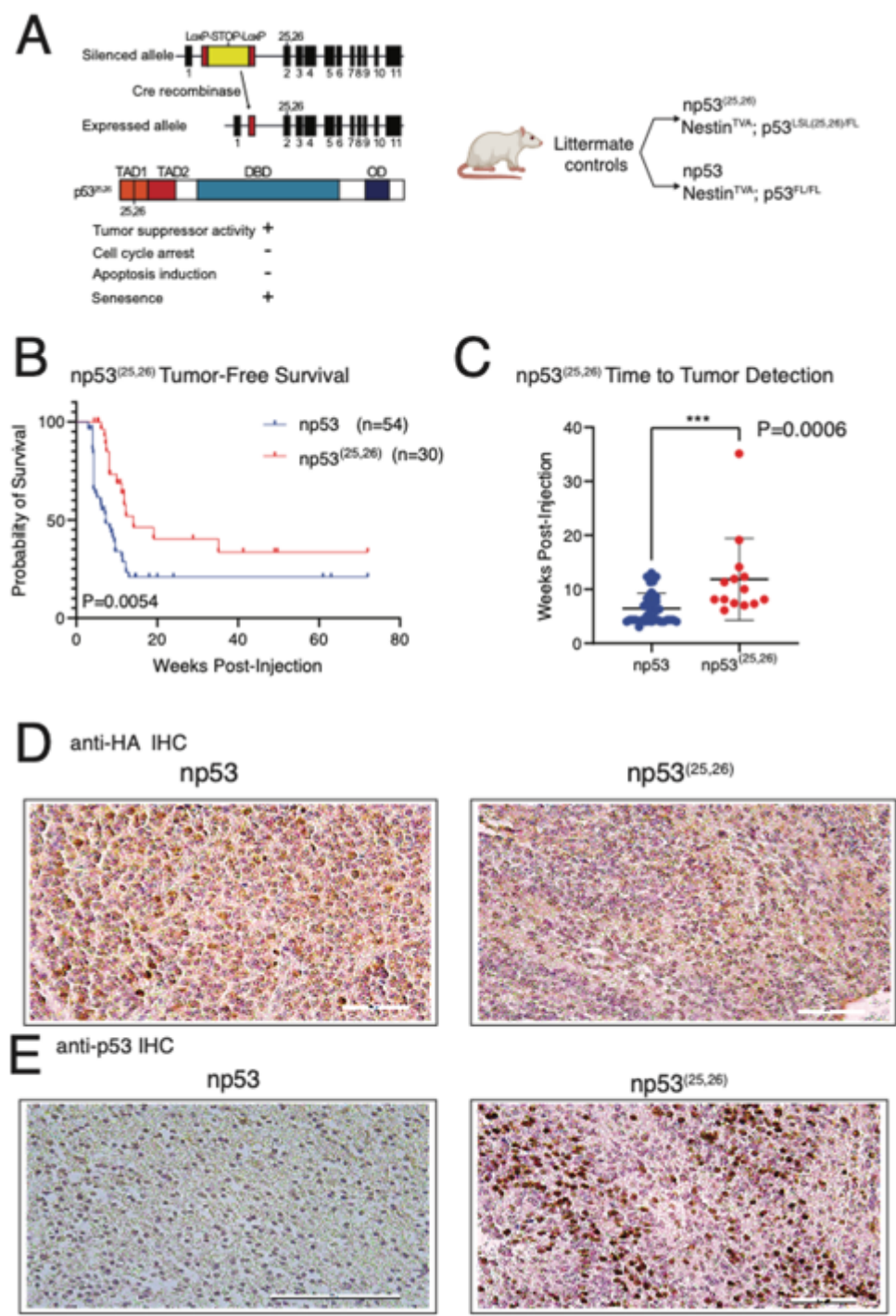


Figure 5. Effect of tumor-specific *Atm* loss in primary DMGs in a *Cdkn1a*-null background (p21^{-/-})

- (A) Overview of p21^{-/-} genotypes analyzed
- (B) Tumor free survival of nlp21A mice with and without intact *Atm* using log-rank test.
- (C) Post-focal brain irradiation survival of nlp21A mice with and without intact *Atm* indicating a statistically significant survival benefit in nlp21A^{FL/+} mice (P-value < 0.05) using log-rank test.
- (D) IHC showing p21 expression in nlp21A mouse brains. Nestin^{TVA}; Pten^{FL/FL}; Atm^{FL/+} (nPtenA) tumor-bearing brain generated with identical RCAS viruses shown as control.
- (E) Plot indicating percentage of tumor cells staining positive for p21 compared to total cell count.
- (F) IHC with Ki67 showing proliferation for nlp21A^{FL/+} and nlp21A^{FL/FL}
- (G) TUNEL staining of tumor-bearing brains of nlp21A mice with and without intact *Atm* in tumors collected one hour post-focal brain irradiation.
- (H) Quantification of TUNEL staining in nlp21A^{FL/+} mice (P-value < 0.05) based on unpaired t-test.

Scale bar = 50uM on IHC.



1094

1095 **Figure 6. Tumor formation in mice expressing a p53 transactivation domain 1**

1096 **mutant.**

1097 (A) Schematic for conditional p53 transactivation domain 1 mutant, and mice
1098 genotypes for expression of a p53 transactivation domain 1 mutant.
1099 (B) Tumor free survival in the np53^(25,26) compared to the np53 control based
1100 on log-rank test.
1101 (C) Time to tumor presentation in the p53^{25,26/FL} group compared to the p53-
1102 FL/FL controls with Wilcoxon test.
1103 (D) IHC for Anti-HA in p53 and p53^(25,26) group. Scale bar = 50 uM
1104 (E) IHC for p53 expression in p53 (Scale bar = 100 uM) and p53^(25,26) (50 uM)
1105 group.

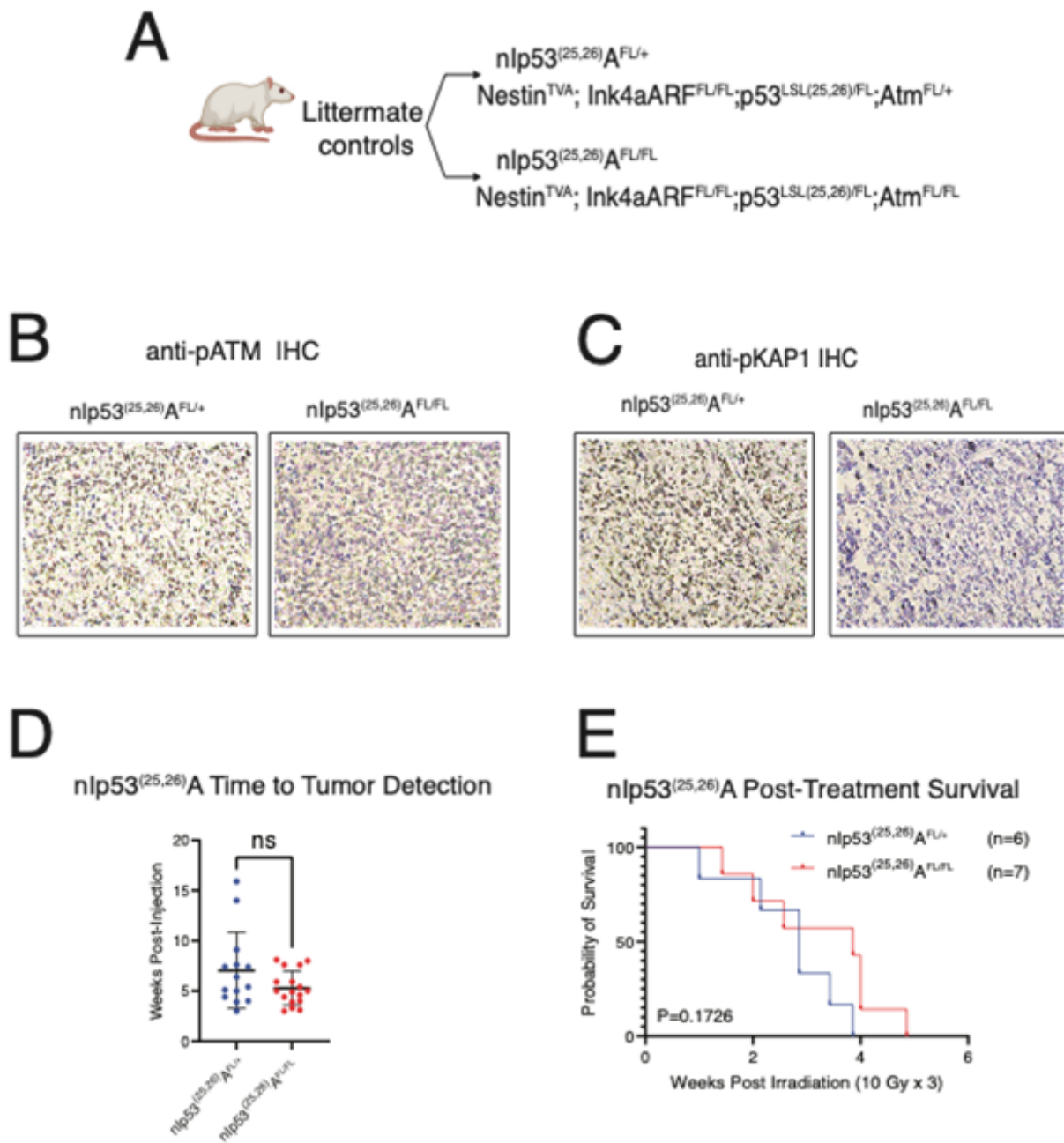


Figure 7. Effect of *Atm* loss on survival after fractionated focal brain irradiation in mouse DMGs expressing a p53 transactivation domain 1 mutant.

(A) Schematic showing p53^{LSL(25,26)} allele and genotypes with Nestin^{TVA-}; p53^{LSL(25,26)/FL-}; Ink4A/ARF^{FL/FL} mice with either Atm^{FL/FL} or Atm^{FL/+}

1115 (B) IHC showing phosphor-Atm in $Atm^{FL/+}$ and $Atm^{FL/FL}$ tumors. Scale bar =
1116 50uM.

1117 (C) IHC showing phosphor-Kap1 expression in $Atm^{FL/+}$ and $Atm^{FL/FL}$ tumors.
1118 Scale bar = 50 uM.

1119 (D) Time to tumor formation in $Nestin^{TVA}$; $p53^{LSL(25,26)/FL}$; $Ink4A/ARF^{FL/FL}$ mice
1120 with either $Atm^{FL/FL}$ or $Atm^{FL/+}$ (dot plot). ns, no statistical significance by
1121 Wilcoxon test.

1122 (E) Overall survival following fractionated brain irradiation in mouse DMGs
1123 expressing a p53 transactivation domain 1 mutation with or with *Atm* loss,
1124 with P-value based on log rank test.

1125
1126
1127
1128
1129
1130
1131
1132
1133

1134 **Tables**

1135

1136 Table 1. Summary of the effect of *Atm* loss on radiation sensitivity in genetically
1137 engineered DMG mouse models.

Genotype (Nestin ^{TVA} + Cre, Luc, PDGFB)	Baseline Radiation Therapy sensitivity	Effect of <i>Atm</i> loss on response to radiation therapy
p53 ^{FL/FL}	Resistant	More sensitive(5)
Ink4A/ARF ^{FL/FL}	Sensitive	No effect(5)
Pten ^{FL/FL}	Sensitive	No effect(11)
p53 ^{FL/FL} ; Ink4A/ARF ^{FL/FL}	Very Resistant	More sensitive(5)
H3f3a ^{LSL-K27m/+} ; p53 ^{FL/FL}	Resistant	More sensitive
p21 ^{-/-} ; Ink4A/ARF ^{FL/FL}	Sensitive	More resistant
p53 ^{LSL-25,26/FL} ; Ink4A/ARF ^{FL/FL}	Resistant	No effect

1138

1139

1140 Table 2 - Key resources table

REAGENT or RESOURCE	SOURCE	IDENTIFIER
Antibodies		
Rabbit polyclonal HA-probe	Santa Cruz Biotechnology	Cat# sc-805 RRID: AB_631618
Mouse monoclonal Ser1981 phosphorylated ATM	MilliporeSigm a	Cat# 05740 RRID: AB_2062670
Rabbit anti-mouse Ser824 phosphorylated Kap1	ThermoFisher	Cat# A300-767A RRID:AB_2779445
Rabbit polyclonal IgG p21	Santa Cruz Biotechnology	Cat# sc-471 RRID:AB_383248
Mouse TotalKap1	Bethyl Laboratories	Cat#A300-775A
Mouse γH2AX	Millipore	Cat# 05-636
Chemicals, peptides, and recombinant proteins		
D-luciferin, potassium salt	Gold Biotechnology	Cat# LUCK-1G
Critical commercial assays		
PicoPure DNA extraction kit	ThermoFisher	Cat# KIT0103
Cell Media and supplements		
Dulbecco's Modified Eagle's medium	ThermoFisher	Cat# 11965092
10% Fetal Bovine Serum	ThermoFisher	Cat# A31604-02

Non-Essential Amino Acids	ThermoFisher	Cat#11140-050
Experimental models: Cell lines		
UMNSAH/DF-1 chicken fibroblast cells	ATCC	CRL-12203™
SF8628 Human Cell line DIPG H3.3-K27M	University of California San Francisco (UCSF)	Developed by Dr. Rintaro Hashizume at UCSF
Experimental models: Organisms/strains		
Mouse: <i>Nestin</i> ^{TVA} : Tg(NES-TVA)J12Ech/J	The Jackson Laboratory	RRID:IMSR_JAX:003529
Mouse: H3f3a-LSL-K27M-Tag	Lab of Dr. Suzanne Baker	N/A
Mouse: LSL-p53-25,26	Lab of Dr. Laura Attardi	N/A
Mouse: p21 ^{-/-}	The Jackson Laboratory	RRID:IMSR_JAX:016565
Mouse: <i>p53</i> ^{fl} : B6.129P2-Trp53tm1Brn/J	The Jackson Laboratory	RRID:IMSR_JAX:008462
Mouse: <i>ATM</i> ^{fl} : 129-Atmtm2.1Fwa/J	The Jackson Laboratory	RRID:IMSR_JAX:021444

Mouse: <i>Ink4a/Arf^{fl}</i> : Cdkn2atm1Rdp	Mouse Genome Informatics	MGI: 1857942
Athymic Mice (rnu/rnu genotype, BALB/c background)	Envigo	Code: 069
Oligonucleotides		
Primers for <i>p53^{fl}</i> alleles	Weidenhamm er et al., 2023	N/A
Primers for <i>Ink4a/Arf^{fl}</i> alleles, see table S1	Weidenhamm er et al., 2023	N/A
Atm recombined probe, 5'- ACACATGCATGCAGGCAGAGCATC CCT-3'	Weidenhamm er et al., 2023	N/A
Atm-floxed probe, 5'- AGCTGTTACTTTTGCCTTTGGTGTG GCG-3'	Weidenhamm er et al., 2023	N/A
p53 recombined probe, 5'- CTTGATATCGAATTCCTGCAGCCC GGG-3'	Weidenhamm er et al., 2023	N/A
p53 floxed probe, 5'- ATGCTATACGAAGTTATCTGCAGC CCGG-3'	Weidenhamm er et al., 2023	N/A

Ink4a/Arf recombined probe, 5'- CATTATACGAAGTTATGGCGCGCC C-3'	Weidenhamm er et al., 2023	N/A
Ink4a/Arf floxed probe, 5'- CTCTGAAAACCTCCAGCGTATTCT GGTA-3'	Weidenhamm er et al., 2023	N/A
Recombinant DNA		
Plasmid: RCAS-Cre	Barton KL, et al., 2013	N/A
Plasmid: RCAS-Luc	Laboratory of Oren Becher	N/A
Plasmid: RCAS-PDGFB	Barton KL, et al., 2013	N/A
Software and algorithms		
ImageJ	NIH	https://imagej.nih.gov/ij/
Prism 7	GraphPad Software Inc.	https://www.graphpad.com/scientific-software/prism/

QuantaSoft	Bio-rad	https://www.bio-rad.com/en-us/life-science/digital-pcr/qx200-droplet-digital-pcr-system/quantasoft-software-regulatory-edition?!ID=1864011
Xenium Analyzer	10xGenomics	https://www.10xgenomics.com/instruments/xenium-analyzer
Seurat	Satija Lab	https://satijalab.org/seurat/
StLearn	Stlearn	https://stlearn.readthedocs.io/en/latest/
Squidpy	Squidpy	https://squidpy.readthedocs.io/en/stable/
STRING	STRING	https://string-db.org
HOMER Motif Analysis	HOMER	http://homer.ucsd.edu/homer
Trimmomatic	Trimmomatic	Version 0.36
Bismark Software	Bismark	Version 0.24.0
Other		
Biological Safety Cabinet	Thermo Fisher Scientific	Cat#13-261-222

IVIS Lumina III In Vivo Imaging System	PerkinElmer	Cat#CLS136334
CO ₂ Incubators	Thermo Fisher Scientific	Cat#4110
EVOS M7000 Imaging System	Thermo Fisher Scientific	Cat#AMF7000
Hamilton Syringe	Hamilton	Cat#84851
Isoflurane Vaporizer	Kent Scientific	Cat#VetFlo-1205S
Oxygen Concentrator	Fisher Scientific	Cat#04-777-122
Sure-Seal Large Mouse/Rat Induction Chamber	World Precision Instruments	Cat#EZ-1785
Sterile Sleeves	VWR	Cat#414004-510
TUNEL DeadEnd Colorimetric System	Promega	Cat#G7360
AZD1390	Astrazeneca	N/A
Mycoplasma Detection Kit	InvivoGen	Cat#rep-mys-10
Short Tandem Repeat	Promega PowerPlex 16 HS System	Cat#DC2101

1141 Materials and equipment

1142 **D-Luciferin Stock Solution**

Reagent	Final concentration	Amount
---------	---------------------	--------

D-Luciferin, Potassium Salt	n/a	1 g
Dulbecco's Phosphate Buffered Saline without Ca^{2+} and Mg^{2+}	1X	66.6 mL
Total	15mg/mL	66.6 mL

1143 Store at -80°C; expires after 1 year

1144

1145 **Alternatives:** D-Luciferin Sodium Salt and L-Luciferin Potassium Salt can be substitute
1146 for D-Luciferin, Potassium Salt

1147

1148

1149